The Potential of Remote LIBS and Raman Spectroscopy for LIDAR Diagnostics and Treatment of Solid Materials

Mats Lundqvist

Diploma Paper
Lund Reports on Atomic Physics, LRAP 341
Lund, May 2005

Abstract

The LIDAR (*LI*ght *D*etection *A*nd *R*anging) technique has been used for atmospheric measurements and fluorescence measurements of solid materials for a long time. In the present work, the technique has been used for elemental analysis by focusing a pulsed laser beam onto metal plates, stones, minerals and crystals at 60 m distance. A glowing plasma was induced on the target surfaces, emitting both continuum light and discrete emission lines. The method is called R-LIBS (Remote Laser-Induced Breakdown Spectroscopy) and is now being developed for planetary exploration, mineral analysis, detection of landmines, laser cleaning, etc. By sweeping the focused laser beam over a target area under computer control, an imaging measurement could be performed. Furthermore, a replica of an Italian statue and an Italian marble statue head replica were cleaned. An oxide-covered copper plate was also cleaned under spectroscopic control. Finally, the course of action when doing future measurements based on the method called remote Raman spectroscopy was discussed. This method gives information on the structure of the investigated material. The present work was performed with the recently upgraded mobile LIDAR system operated by the Atomic Physics Division of the Lund Institute of Technology. A new system for target area TV surveillance and a peak identification software were also developed as part of the project.

Sammanfattning

LIDAR-tekniken (*LI*ght *D*etection *A*nd *R*anging) har länge använts för att utföra atmosfäriska mätningar och fluorescensmätningar på fasta material. I denna studie har tekniken använts för elementanalys av metaller, stenar och kristaller genom att fokusera en pulsad laserstråle på materialets yta på 60 m avstånd. Ett lysande plasma skapades på ytan, som strålade ut ljus med ett kontinuerligt spektrum som även innehöll diskreta emissionslinjer. Denna metod kallas R-LIBS (fjärr-laserinducerad nedbrytningsspektroskopi) och utvecklas runt om världen för applikationer inom planetutforskning, mineralanalys, detektion av landminor, laserrengöring, etc. Genom att svepa den fokuserade laserstrålen över ett målområde kunde en avbildande mätning utföras. Vidare har fjärrengörning av en trädgårdsstaty och ett statyhuvud tillverkat av marmor utförts. Även en oxiderad kopparplåt kunde rengöras under spektroskopisk kontroll. Slutligen har tillvägagångssättet för framtida mätningar med metoden fjärr-Raman spektroskopi diskuterats för att kunna bestämma ett materials struktur. Detta projekt har utförts på det befintliga och nyligen uppgraderade mobila LIDAR-systemet på avdelningen för Atomfysik vid Lunds Tekniska Högskola. Till detta system har även ett nytt system för TV-övervakning av målområdet, samt mjukvara för identifiering av toppar i spektra utvecklats.

Contents

Chapter 1

Introduction

This diploma paper for the degree of Master of Science was carried out at the Atomic Physics Division of the Lund Institute of Technology. The aim of the thesis was to investigate the possibilities of performing remote elemental analysis on targets using Remote Laser-Induced Breakdown Spectroscopy, R-LIBS, with the exisiting LIDAR system. With this method the elemental composition of the target material can be determined by aiming a pulsed focused laser beam at the remotely positioned surface. No information about the molecular structure is obtained due to the optical breakdown and ionisation of the material by the use of this method. Therefore, a complementary technique called Remote Raman Spectroscopy was proposed to be studied and if possible, depending on the timetable of the thesis, some measurements might also be performed. Because of long delays with delivery of optical components and also delays from the mechanical workshop, only the R-LIBS part fitted in the timetable. Instead, the possibility of performing remote ablative cleaning of statues using the LIBS beam was investigated.

The outline of the thesis is given below. In Chapter 2, the fundamental theory behind light interaction and lasers is presented before the basics and applications of remote laser-induced breakdown spectroscopy are discussed. An overview of Raman spectroscopy and its remote applications is also given in this chapter. In Chapter 3, a description of the equipment is included, where also the development of a detection unit and a peak identification program is presented. The remote LIBS measurements and the remote cleaning procedures are described in Chapter 4, together with a discussion on how to perform Raman measurements. Finally, conclusions and a discussion about future work are included in the thesis.

Chapter 2

General Background and Theory

2.1 Introduction

In this chapter the theory behind light interaction with matter, such as absorption, emission and scattering (Sect. 2.2), is explained. Also, a quick description of the Nd:YAG laser, Q-switching and frequency conversion is included together with the historical background of the laser (Sect. 2.3). Finally, the theory, remote operation and applications of LIBS (Sect. 2.4) and Raman spectroscopy (Sect. 2.5) are covered.

2.2 Light Interaction

Light interacts with atoms and molecules in many different ways and the different situations are described below. Important information can be obtained by examining the emitted or scattered light, such as the electronic configuration, molecular structure, etc.

2.2.1 Absorption

When the incoming photon with the wavelength λ and energy $E = hc/\lambda$ matches a transition from the ground level to an excited level of an atom or molecule, the photon is absorbed and the electron is promoted to an excited state. The absorption process is strongly dependent on the absorption lineshape (temperature, pressure) and the absorption linestrength (transition probability, level population, species concentration). From the excited level the electron can be de-excited through radiative or non-radiative processes (see below) [1]. The electron can also be excited from the ground level to an upper level by simultaneously absorbing N photons. This process requires

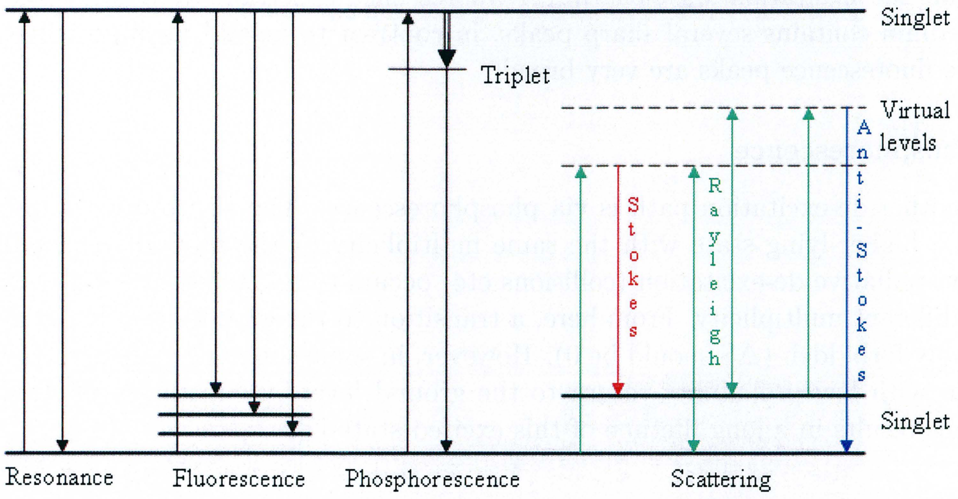

Figure 2.1: Light/matter interaction

high laser powers due to the P^N dependence of the multi-photon absorption probability, where P is the laser power and N is the number of absorbed photons. If the total energy of the absorbed photon(s) exceeds the ionisation limit, the electron will become free and the atom will be ionised [2].

2.2.2 Emission

Resonance Radiation

An atom or molecule in an excited energy level of the atom, can return to the ground level by spontaneous or stimulated emission of light. The wavelength of the emitted photon is identical to the wavelength needed to promote the electron to the excited state by absorption. Due to the nature of spontaneously emitted light, the radiation is sent out in random directions. In the case of stimulated emission, a photon is sent out in the same direction as the one of the incoming stimulating photon and with the same phase. This is the fundamental mechanism for lasing action.

Fluorescence Radiation

Instead of returning to the ground level as in resonance radiation, the electron can also be de-excited to several higher-lying energy levels. Thus, the emitted light spectrum includes peaks with photon wavelengths at lower energies than the excitation wavelength. A fluorescence spectrum from a gaseous medium contains several sharp peaks, in contrast to a solid medium where the fluorescence peaks are very broad.

Phosphorescence

Another de-excitation path is via phosphorescence. The electron is excited to a higher-lying state with the same multiplicity as the ground level, but non-radiative de-excitation (collisions etc) occurs to a lower-lying level with a different multiplicity. From here, a transition to the ground level is radiatively forbidden (ΔS should be 0). However, in some substances the electron can with low probability return to the ground level by emitting a photon. This results in a long lifetime of this excited state [2].

2.2.3 Scattering

Rayleigh and Raman Scattering

When the incident radiation does not match a transition between two energy levels in an atom/molecule, there is still a small probability that the electron is promoted to a virtual energy level. From here the electron is quickly de-excited to the ground level (elastic scattering) yielding Rayleigh scattering. If the ground level contains several sublevels there may exist a wavelength shift compared to the excitation wavelength (inelastic scattering) and the process is referred to as Stokes or Anti-Stokes Raman scattering, depending on the sign of the shift. Further details are given in Sect. 2.5 on page 17.

Mie Scattering

If the incident light has a much smaller wavelength than the particle size, the observed emission is called Mie scattering and follows an approximate $1/\lambda^2$ dependence. The occurrence of the blue sky and the red sunset arises from Mie and Rayleigh scattering due the stronger scattering of photons with shorter wavelengths. Also, the rainbow phenomenon can be explained by Mie-scattering theory.

2.3 Lasers

2.3.1 History

Theodore Maiman constructed the first working laser, a ruby laser, in June 1960. The word LASER is short for Light Amplification by Stimulated Emission of Radiation. The fundamentals of the laser technique have their origin in the development of the MASER (Microwave Amplification by Stimulated Emission of Radiation). One could say the laser is a maser in the optical regime. Many new kinds of lasers have been developed since 1960 - for example gas (HeNe, CO_2), solid-state, semiconductor, excimer, dye lasers, etc. [3].

2.3.2 The Nd:YAG Laser

One of the most important lasers, the Nd:YAG laser, was built at Bell Labs in 1964. Neodymium, Nd^{3+}, is doped into a yttrium-aluminium garnet ($Y_3Al_5O_{12}$). The ground state of the Nd^{3+} ion is the $^4I_{9/2}$ level and there are two main pump bands around 730 and 800 nm which are coupled by fast non-radiative decay to the upper laser level $^4F_{3/2}$. Nd:YAG lasers are usually pumped by a Xe-arc flash lamp. The ion can decay (either by spontaneous or stimulated emission) to many different lower lying ^4I levels (J=15/2, 13/2, 11/2, 9/2). The lifetime of the upper laser level is very long, $\approx 230\ \mu s$, since electric dipole transitions to lower levels are forbidden (ΔJ should be 0 or ± 1), but become weakly allowed due to crystal-field interaction. The strongest transition is to the $^4I_{11/2}$ level and corresponds to $\lambda = 1.064\ \mu m$. This is the most widely used lasing wavelength of Nd:YAG lasers. The lower laser level is quickly depleted by non-radiative decay and the ion is again situated in the ground level. Additionally, Nd:YAG lasers can be made to produce radiation at 532 nm, 355 nm or 266 nm, by frequency doubling/tripling and mixing through non-linear processes in crystals. It can also be mode-locked and Q-switched [4]. Some of these techniques are discussed below. The fact that it has reasonably small dimensions and low maintainance requirements makes it useful for mobile installations.

2.3.3 Q-Switching

The cavity Q factor, quality factor, is defined as

$$Q = 2\pi \times \frac{\textit{energy stored}}{\textit{energy lost in one oscillation cycle}} \tag{2.1}$$

By preventing laser action with a shutter, a large population inversion can be built up due to the absence of stimulated emission which normally depopulates the excited state. The energy stored in the cavity in form of photons is then low and the cavity losses are large. This corresponds to a low Q value. When the shutter is opened, a very short and intense laser pulse is released out of the cavity. The energy loss is then low (determined by the end-mirror power reflectivity) and the energy stored in form of photons in the cavity is high which results in a high Q factor. Thus, Q-switching means switching of the cavity Q factor from a low to a high value. The pulse length is in the nanosecond range and the peak power is in the MW range [4].

2.3.4 Frequency Conversion

Polarization of an optical medium occurs when an applied alternating electric field is displacing the outer electrons while leaving the nuclei and inner electrons practically uneffected. The polarization P of a medium by an electric field E is given by Eq. 2.2.

$$P = \epsilon_0(\chi_1 E + \chi_2 E^2 + \chi_3 E^3 + \ldots), \tag{2.2}$$

where χ is the susceptibility and ϵ_0 is the vacuum permittivity. In the normal case when the displacements are small, the first linear term is totally dominating. Only at very high laser powers in non-isotropic optical materials (lacking inversion symmetry) the second and third order terms will become important. If the electric field is described by a cosine function with an amplitude E and an angular frequency ω, $E_0\ cos\ \omega t$, the resulting polarization will include a term proportional to $cos\ 2\omega t$ due to the quadratic term in the equation. Thus, the oscillating polarization will generate electromagnetic radiation at the angular frequency 2ω in addition to the much stronger radiation at the fundamental frequency. A similar argument results in a term proportional to $cos\ 3\omega t$ when the third order term is included in the calculations.

When two laser beams with different frequencies (ω_1, ω_2) are interfering in a non-linear material, the quadratic term of the polarization produces harmonics at $2\omega_1$ and $2\omega_2$, but radiation at $\omega_1 - \omega_2$ and $\omega_1 + \omega_2$ is also obtained. The latter phenomenon is called *frequency mixing* and can also be produced by the third order term, giving rise to many more possible frequency combinations when even more beams are interfering [5]. Another frequency mixing process is called *parametric amplification* and is further discussed in Sect. 3.3.1.

2.4 Laser-Induced Breakdown Spectroscopy

2.4.1 Introduction

Laser-induced breakdown spectroscopy (LIBS) is a quasi-nondestructive method, where intense focused laser pulses, typically from a Q-switched Nd:YAG laser, are directed towards a target sample (in solid, liquid or gas state - see Fig. 2.2). A plasma (also called "laser spark") is created and the emitted light is analysed with a spectrometer to determine the elemental composition of the target sample. Elemental concentrations are determined by building a calibration curve of the signal versus the concentration in samples of known composition. By using a delay generator connected to the gated detector, the time window for detection can be freely chosen. This also causes suppression of the background light and enhances the signal. LIBS is sometimes also referred to as LIPS, Laser-Induced Plasma Spectroscopy.

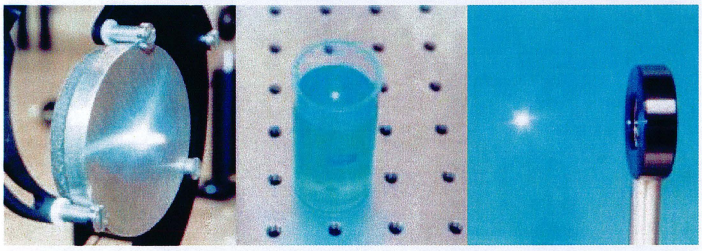

Figure 2.2: LIBS in different media (From [6])

2.4.2 Plasma Generation

A plasma is a high temperature ionized gaseous state with macroscopic charge neutrality. The material within the spark is the result of ablation (i.e. atomization) of a small amount of target material. The initial part of the laser pulse forms a high-electric field region and heats the sample followed by vaporization of a small amount of the surface. Also single- and multi-photon absorption occurs. The vaporization process is slow compared to the energy deposition rate of the laser pulse; consequently the underlying material is also heated and a critical pressure is reached where the surface explodes (ablation). At high temperatures the ablated material is partly ionized, although the high ion concentration is mainly due to the interaction between the ablated material and the laser radiation. The result is a plasma cloud situated close to the sample surface. In the central region the temperature is at its highest (mostly ionized atoms) while the surrounding regions are colder, thus containing a larger density of neutral atoms and molecular species (see Fig. 2.3). If a long laser pulse (ns pulse or longer) is used, plasma heating may occur due to inverse Bremsstrahlung absorption, which increases the temperature even further and a higher amount of the vaporized material is ionized [7, 8]. The plasma generation is in reality much more complex with more factors to consider. The description above is, however, sufficient for the purpose of understanding the later parts of this diploma thesis.

Although the peak power of the laser is very high (in the megawatt range), the average power is typically a couple of watts. This means that the laser interaction with the sample at large causes no increase in sample temperature, resulting in virtually no damage to the material. Still, typical plasma temperatures obtained locally are in the range 10.000 K to 20.000 K. The characteristics of the plasma depend on the chemical composition of the target, laser wavelength, pulse energy and length, gas pressure etc. The irradicance required to induce plasma formation is on the order of 10^8 W/cm^2 [9].

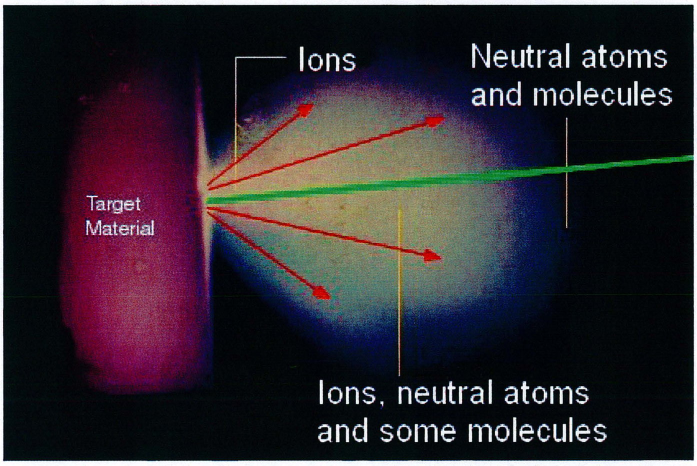

Figure 2.3: Plasma generation (Modified from [7]).

2.4.3 Time-Resolved Spectral Analysis

The laser-induced plasma has a lifetime of a couple of tens of μs, which is significantly longer than the laser pulse duration. Thus, the changes in the plasma and the emitted light occur on a microsecond timescale.

The plasma emits an intense light continuum covering a region from soft X-rays through the visible to the near IR (infrared). The mechanisms responsible for the broad energy spectrum are Bremsstrahlung (electron energy loss during deceleration) and recombination (electron-capturing by ions) and the light is emitted in all directions. As the plasma cloud expands outwards at supersonic speeds, it is cooled down by radiation losses and interaction with the atmosphere. The plasma continuum decreases and fluorescence light from the excited atoms and ions is seen on the spectrometer as they return to lower energy states. The ion lines quickly disappear and the only peaks left are those belonging to excited neutral atoms. At a certain point in time the emission lines from the excited neutral atoms reach a maximum intensity and are readily identified.

Line-Broadening Mechanisms

The width of the LIBS peaks changes in time due to Doppler broadening, collisional broadening and broadening due to the Stark effect. The Doppler broadening arises from the fact that atoms travel with different velocities in the plasma. The lineshape is Gaussian, which is common for inhomogenous line-broadening mechanisms. Collision broadening (also called pressure broadening) occurs due to collisions between radiating atoms and other particles (atoms, ions, electrons and lattice phonons) resulting in a Lorentzian lineshape, which is common for homogenous line-broadening mechanisms. The combined lineshape, when both Doppler and collision broadening contribute to the line-broadening, is called a Voigt profile. The natural linewidth of a peak is obtained from fundamental quantum mechanical calculations of the spontaneous decay, which state that the minimum width of a peak is inversely proportional to the decay time. The shift in a spectral line due to electric fields is called the Stark shift. These electric fields are originating from nearby particles (ions and electrons) and cause local variations of the energy levels, resulting in Stark broadening.

2.4.4 Advantages/Disadvantages

Advantages and disadvantages of LIBS compared to more conventional elemental analysis methods are included in the table below [10]:

Advantages	*Disadvantages*
Rapid analysis (one measurement/pulse – total analysis time is determined by the number of integrated shots)	Detection limits (1 to 100 ppm) are generally not as good as for established techniques
Simultaneous multi-element detection	Spectroscopic interferences among lines of different trace elements
Ability to detect all elements (high and low Z)	Possibility of ocular damage by the high-energy laser pulses
Ability to clean dust or weathered layers off of sample surfaces	Particle size and matrix effects (e.g. sample composition, homogeneity, and moisture contents)
Standoff analysis capability (only optical access needed)	
No need for sample preparation	
Field portable	
Practically non-destructive ($\sim$0.1 μg to 1 μg vaporized)	

Dual Laser Pulses

One way to improve detection limits is to use two laser pulses and create breakdown in the air near the sample surface, only heating it slightly with the first pulse and then create a plasma plume in front of the sample with the second pulse. The plasma then interacts with the air plasma and a stronger emission signal is achieved. A second method is to first create breakdown in the sample itself so that a plasma plume is formed and then let the second pulse interact with the created plasma, which also leads to an improved signal strength [11].

Ultra-Short Pulses

Ultra-short ($\sim$ fs) pulses produce less thermal damage around the ablation region, resulting in very precise holes. This is due to the direct transition of material to the vapor or plasma phase through multi-photon absorption, without melting.

$$Power\ density = \frac{Power}{Area} = \frac{Pulse\ energy/Pulse\ duration}{Beam\ area} \tag{2.3}$$

According to Eq. 2.3, the power density produced at the target surface is increased when using shorter pulse durations in comparison to longer pulses ($\sim$ ns). Thus, the plasma threshold is much lower in terms of laser pulse energy and much lower pulse energy can be used for LIBS measurements. In combination with the fact that there is no plasma reheating, this also results in a much smaller plasma. Other femtosecond excitation advantages are lower continuum background and faster plasma dissipation, which combined with using a high pulse repetition rate may allow non-gated detection [12]. Measurements with ultra-short pulses have been performed within a French-German project, called Teramobile, where a mobile terawatt laser, capable of producing 75 fs pulses with 350 mJ energy, is incorporated into a standard freight container [13].

2.4.5 Remote LIBS

For remote analysis applications (Remote LIBS), there are two basic types of LIBS instruments differing only by the method of delivery and collection of the laser and plasma light respectively. One method uses an optical-fibre probe configuration and is suitable for applications where no optical line-of-sight access to the material is possible. The laser-induced radiation is then collected by the same fibre or by other optical fibres and is brought back to the detection system. The core diameter of the fibre has to be sufficiently large so that the light power density does not exceed the damage threshold [14]. The other method uses an optical telescope arrangement and is suitable for applications where there is line-of-sight access to the material. The laser beam is transmitted through a focusing lens and the laser-induced radiation is collected by the telescope. Damage to the output mirrors or other optical components when using high energy pulses may occur.

The distance that can be achieved depends on characteristics of the laser and the optics used to focus the pulses on the target to produce a high power density. A laser with a good Gaussian profile allows focusing to a near diffraction-limited spot. The tighter the focus, the less energy is required to produce the laser-induced breakdown. A wavelength in the UV (ultraviolet) is often used instead of longer wavelengths, since shorter wavelengths make it possible to achieve a spark with much lower pulse energy [13]. This is related to the increased probability of ionisation through single- and multi-photon absorption.

2.4.6 Remote LIBS Applications

Mining

Mining operations require laboratory-based analysis, where an ore sample must be collected from the site, which increases the transport costs and the risk of contamination and error. The spectroscopic method normally used is X-ray fluorescence (XRF), containing radioactive sources and has low sensitivity when measuring some elements (low Z). The analysis is also more time consuming than an analysis of a LIBS measurement. When the ore is analyzed in the laboratory, the extracted data must be sent back to the ore extraction point. Using LIBS to do real-time measurements of the ore quality improves the efficiency of mineral ore extraction. As mentioned in Sect. 2.4.4, LIBS is capable of measuring virtually all inorganic elements. Accordingly, the LIBS technique can be used in all mining applications [15, 16].

Laser Cleaning

LIBS can be utilized in laser cleaning to give an analysis of the ejected material at each ablation step - spectroscopic guidance. If the contaminant layer is removed and ablation occurs on the clean surface, the LIBS spectra will show a change in composition of the ejected particles and thus can act as a control system. On some materials the cleaning process is self-terminating and is consequently very “safe“. Laser cleaning of cultural buildings and statues, where algal growth or other substances were attached to the material, has been successfully performed by different groups [17]. Also removal of graffiti paintings on walls and trains has been demonstrated [18].

Planetary Exploration

Several space missions are planned to land rovers on asteroids, comets, the Moon, and Mars. The goal is to increase the scientific return of these missions by developing new methods to be able to perform more analyses per mission [19]. Remote LIBS is under development as part of the Mars Instrument Development Program (MIDP). In previous missions to Mars all examined rocks were contaminated with a dust layer. Fortunately, LIBS has the capability to remove dust and other surface material and the progress can be monitored due to the change in LIBS signal when the clean rock is reached. The rapid sample acquisition by just aiming the laser and refocusing on a new target makes it more convenient than moving the rover to a new location. Also targets can be analysed, which cannot be reached by the rover itself. The behaviour of the plasma under Martian conditions, 5-7 Torr CO_2 atomsphere, is different in comparision to LIBS experiments performed on earth due to different atmospheric composition and pressure. The lower pressure results in a faster expansion of the plasma which leads to reduced shielding of the target surface. Thus, more material is ablated per pulse and a stronger signal is achieved. LIBS conditions can vary from atmospheric pressures (approx. 750 Torr) to vacuum, with a maximum efficiency between 10 and 100 Torr [10].

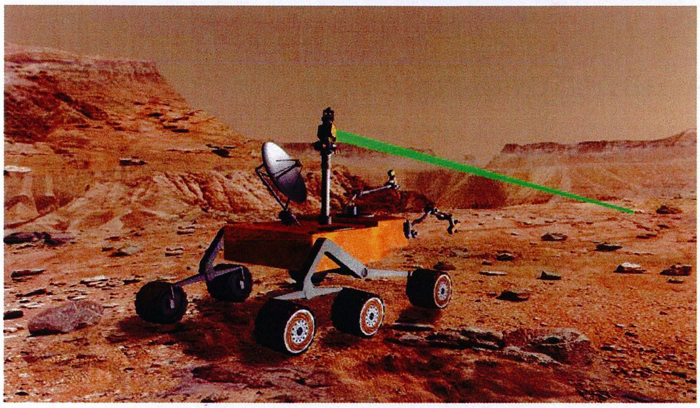

Figure 2.4: Mars exploration (Modified from [20]).

Hazardous Materials and More

Removing a sample of a nuclear reactor component for laboratory analysis may endanger the physical stability of the reactor and the overall security. It is also a costly and time consuming procedure where a large number of samples are required. LIBS has several advantages, such as its non-sensitivity to gamma radiation in comparison to X-Ray Fluorescence (XRF), the reactor component can be surrounded by liquid and the possibility of remote operation which is crucial in radioactive/high temperature/toxic environments. In situations when there is no line-of-sight to the material an optical-fibre probe is used [21]. Detection of landmines can be performed by directing a pulsed LIBS beam onto a suspicious object, possibly a landmine casing, and thereby analyzing the composition. The collected spectrum must then be compared with a database containing spectra from different landmines [22].

The contained explosive charge may be determined with Remote Raman Spectroscopy (Sect. 2.5). Other possible applications are remote detection of anthrax spores by selectively attaching heavy metal atoms [23], monitoring of alloy composition in the steel industry [24] and identification of radioactive nuclear waste.

2.5 Raman Spectroscopy

2.5.1 Introduction

The Indian scientist C.V. Raman first observed the Raman effect in the end of the 1920s. For this he received the Nobel prize in 1930. Raman scattering was discussed in Sect. 2.2.3.

2.5.2 Classical Theory

An atom becomes polarized in a homogeneous electric field due to the displacement of the electronic cloud compared with the nucleus. The polarizability constant α is a proportionality constant between the induced electric dipole moment $\vec{P}$ and the applied electric field $\vec{E}$. In a molecule α is replaced by a polarization tensor because of the asymmetric structure of the molecule. As in the case of the atom, an electric dipole moment $\vec{P}$ is induced in the molecule when it is subject to an electric field $\vec{E}$.

$$\vec{P} = \alpha\vec{E} \tag{2.4}$$

If an oscillating electromagnetic field, $\vec{E} = \vec{E}_0 sin(2\pi\nu t)$, is incident on a molecule, the electric field induces an electric dipole moment in the molecule, which varies at the frequency of the incoming field. Then the molecule itself will start radiating at the same frequency because of the varying polarization.

$$\vec{P} = \alpha\vec{E}_0 sin(2\pi\nu t) \tag{2.5}$$

This radiation is called Rayleigh scattering and is elastic in nature. The radiated energy has a $1/\lambda^4$ dependence, which results in an increasing intensity for shorter wavelengths. This was first showed by Lord Rayleigh in 1871. Because of the rotational and vibrational motions of the molecule, the polarizability varies with time.

$$\alpha = \begin{cases} \alpha_0 + \alpha_{lv} sin(2\pi\nu_{vibr}t) & \text{(vibration)} \\ \\ \alpha_0 + \alpha_{lr} sin(2\pi 2\nu_{rot}t) & \text{(rotation)} \end{cases} \tag{2.6}$$

The external oscillating field will couple to the internal oscillation and sidebands to the Rayleigh line will appear in the spectrum. These are called Stokes and Anti-Stokes lines depending on whether they have been down- or upshifted from the Rayleigh frequency. Their line strength is much weaker in comparison to the Rayleigh line (1/1000).

$$|P| = \begin{cases} \alpha_0 E_0 \sin(2\pi\nu t) + \frac{1}{2}\alpha_{lv} E_0[\cos 2\pi(\nu - \nu_{vibr})t - \cos 2\pi(\nu + \nu_{vibr})t] \\ \\ \alpha_0 E_0 \sin(2\pi\nu t) + \frac{1}{2}\alpha_{lr} E_0[\cos 2\pi(\nu - 2\nu_{rot})t - \cos 2\pi(\nu + 2\nu_{rot})t] \end{cases} \tag{2.7}$$

Typically, only one part in a thousand of the total intensity of incident light is Rayleigh scattered, while for Raman scattering this value drops to one part in a million (0.0001 percent) [2].

2.5.3 Quantum Mechanical Theory

In the quantum mechanical model, virtual levels are introduced and the electrons being situated in the lower, real energy levels (electronic, vibrational and rotational states) are excited to the virtual levels from where they quickly fall down to any of the real levels (see Fig. 2.1). The excitation to a virtual level is temporarily allowed due to the Heisenberg uncertainty relation ($\Delta E \cdot \Delta t \geq \frac{\hbar}{2}$), which states that the energy uncertainty ΔE while determining an energy level is large when a very short time period Δt is considered (see Fig. 2.5). The energy uncertainty of the upper real level is large enough to even cover the ground state. Because of the higher population of the lower levels (Boltzmann distribution), the Stokes lines will be more intense than the Anti-Stokes lines.

2.5.4 Remote Raman Spectroscopy

Remote LIBS and Remote Raman spectroscopy are two complementary techniques. The LIBS method gives information on the elemental composition of the target area and the Raman method gives information on the elemental structure (the bonds between the atoms/molecules). They use essentially the same instrumental components, but the main difference is a filter to block the Rayleigh scattered laser light. Additionally, when switching from doing LIBS measurements to Raman measurements the laser power density must be reduced to prevent plasma generation. The plasma signal is very strong and makes the Raman signal impossible to detect. This can be done by decreasing the laser power or by defocusing the laser beam [10]. The distance

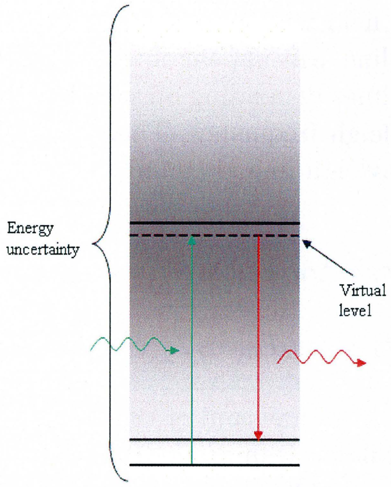

Figure 2.5: Scattering and the Heisenberg uncertainty relation

from the laser/detection system to the detection point is in the range of a few meters up to 100 meters. Raman analysis spots can in addition cover larger areas than LIBS spots.

2.5.5 Analysis of Raman Signals

The Raman effect is very weak, which makes it hard to detect the Raman lines as they are added to the fluorescence signal. A solution is to use longer excitation wavelengths to suppress the fluorescence signal. This would, however, result in a much weaker Raman signal due to the inverse fourth power dependence on the excitation wavelength. A small shift ($\Delta\lambda$ ~1 nm) in excitation wavelength hardly changes the fluorescence signal, but the Raman spectrum will be displaced with the same shift. By collecting two different spectra of the sample with two close-lying excitation wavelengths and subtracting them, a derivative-like graph of the Raman signal is obtained. The two excitation pulses should be matched to give the same signal strength [25].

2.5.6 Remote Raman Applications

Cultural Heritage

Due to the large amount of sulphur dioxide and carbon monoxide released in the atmosphere by burning fossile fuel, many of the statues and historical buildings of cultural interest are chemically modified by acid rain. The sulphuric acid reacts with the calcium carbonate of the marble or other limestone to form gypsum in the superficial layers. The chemical reaction is [26]:

$$CaCO_3 + H_2O + H_2SO_4 \Rightarrow CaSO_4 + 2H_2O + CO_2 \tag{2.8}$$

The gypsum layer is softer than the original stone substrate and accumulates large amounts of water. The black crusts often seen on stone surfaces are hydrocarbons and other pollutants attached to the gypsum spots. The overall pollution grade of a stone surface can be determined with Raman spectroscopy. A line belonging to a symmetric stretch mode of the carbonate ion in calcite can be found in the Raman spectra. This Raman line is Stokes shifted by 1085 cm^{-1} from the laser exciting line. Gypsum, on the other hand, has a strong Raman line at 1007 cm^{-1}.

Mineral Analysis

Remote Raman spectroscopy has the capability of determining mineralogical data at typical LIBS stand-off distances. It may also be used complementary to Remote LIBS when the breakdown threshold of the mineral surface is very high and no plasma can be generated. Most carbonates, sulfates, nitrates, phosphates, silicates, oxides, sulfides and hydroxides have characteristic Raman spectra. Shifts in Raman peak positions can give data on mineral composition, e.g. elemental ratios. Most other techniques used suffer from broad overlapping spectral peaks, which make it difficult to analyse the spectrum. However, Raman spectra show narrow peaks when using a high resolution spectrometer, which rarely overlap.

Planetary Exploration

The search for present or former extra-terrestrial lifeforms (funghi, algae, etc) on other planets may be performed by Remote Raman spectroscopy from rovers. The carotenoid pigment has a strong Raman line at 1130 cm^{-1} in the spectrum and minerals containing it may have biogenic origin [27]. Also chlorophyll and other biomarkers can be detected. A disadvantage of the mentioned method is the incapability of removing dust layers and other crusts covering the target surface. Consequently, the Raman signal might show the mineralogy of the dust and not the hidden rock. These layers have to be removed with other methods, such as laser ablation, to achieve a clean surface. Also, Raman spectroscopy should work equally well at any pressure (from atmospheric pressures to vacuum), because no ablation of the material surface or plasma generation is required as in the LIBS case.

Explosives

Explosives have up to recently only been detectable with techniques like X-ray diffraction, chromatography, mass spectrometry, and Fourier Transform IR/Raman Spectroscopy. These methods require sample preparation and are time-consuming, requiring laboratory analysis. Remote Raman spectroscopy might, on the other hand, instantaneously detect explosives at considerable distances, without sample preparation and in different mixtures. Most likely, the method using an optical fibre to guide the laser beam and collect the laser-induced light will be used due to the low concentrations of the explosive material and the low scattering cross-section of the Raman process. Explosive compounds like HMX, RDX, TNT, NQ, etc. have sharp Raman peaks which simplify the remote detection [28].

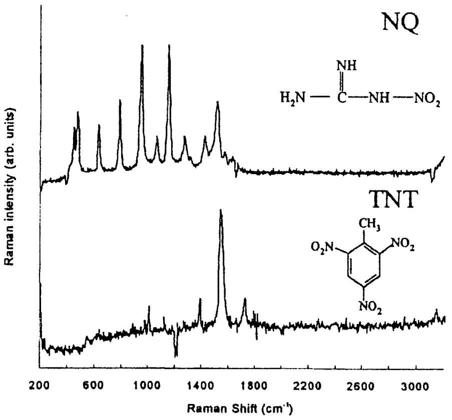

Figure 2.6: Raman spectra of explosives (From [28]).

Chapter 3

Equipment

3.1 Introduction

In this chapter an overview of the Lund LIDAR (LIght Detection And Ranging) system is given (Sect. 3.2). In addition, a thorough description of the transmission system (Sect. 3.3) and the detection system is presented together with several improvements (Sect. 3.4). Also, new software was developed and is discussed in Sect. 3.5.

3.2 Overview

The Lund LIDAR System is a remote scanning system built into a Volvo F610 truck for mobile operation with the use of a Diesel powered electric generator. For stationary operation at the Lund Institute of Technology, the truck is docked to the wall of the LIDAR laboratory room. It consists of two Nd:YAG lasers, an OPO (Optical Parameter Oscillator), an IR-mixing unit, an optical multichannel analyser (OMA), a calibration unit, a vertically mounted 40 cm diameter on-axis Newtonian telescope (f = 1 m), miscellaneous electronics and power supplies. A computer system is used to control the entire system and an overview of the target area is presented on two TV monitors via a sophisticated video surveillance system.

The truck is equipped with an air-conditioning system to maintain a stable temperature for proper laser operation (mainly required for the OPO). The air-conditioning system can handle outside temperatures between -20 to $+30\,^{\circ}$C while keeping the inside temperature constant within $\pm 2\,^{\circ}$C. With four hydraulic support legs the truck can be stabilized to achieve a lower sensitivity to movements of the staff in the floor area [29].

The computer system is based on four network-connected Windows machines running on software written in LabView (National Instruments Corporation). LabView is a graphical programming language where, instead of writing the programming in a text editor, the code is "drawn" [29]. An overview of the entire truck is presented in Fig. 3.1.

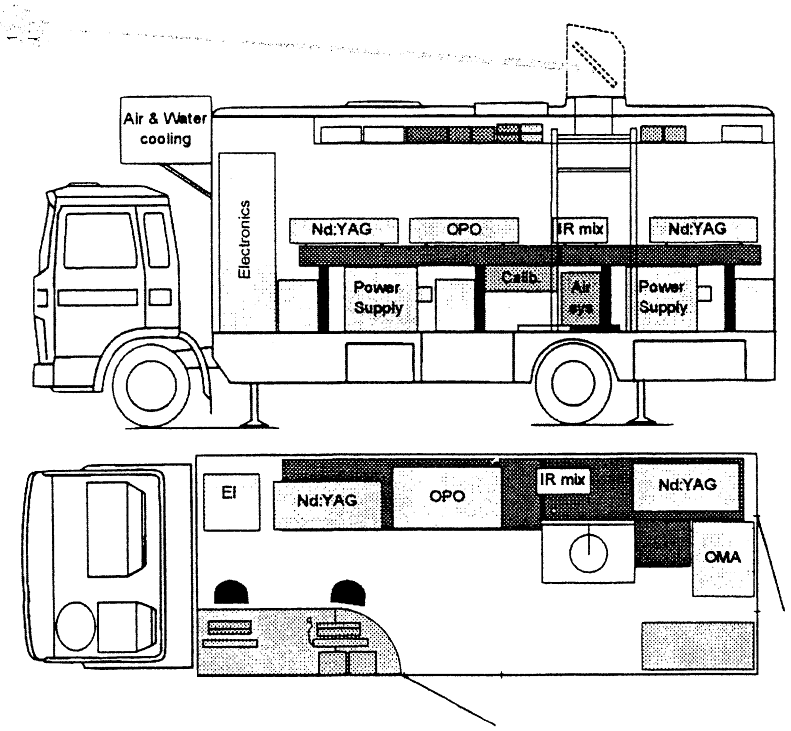

Figure 3.1: The Lund LIDAR system (Modified from [29]).

3.3 The Transmission System

Here the parts of the system involved in producing laser light (Sect. 3.3.1) and transmitting the light (Sect. 3.3.2) are discussed. Finally, the video surveillance system is discussed together with a presentation of a new and improved system (Sect. 3.3.3).

3.3.1 The Laser System

The two Nd:YAG lasers (Spectra Physics Model GCR-290) are Q-switched (see Sect. 2.3) and operate at a 20 Hz repetition rate. They are triggered by an advanced trigger system to ensure proper synchronization with each other. One of the lasers is operating at the frequency-tripled wavelength of 355 nm (other wavelengths are directed into optical terminators) and the other emits laser pulses at the fundamental wavelength 1064 nm. The lasers are used to pump the OPO (a modified Quanta-Ray MOPO-730) and the IR-mixing unit to produce light pulses in the wavelength ranges 220-690 nm, 730-1800 nm and 2600-4300 nm. These units are based on non-linear processes in BBO (β-Barium Borate) and Lithium Niobate ($LiNbO_3$) crystals. In the OPO, one photon at $\lambda = 355$ nm is split into two photons with longer wavelengths resulting in two output beams called the signal (strong) and idler beam (less powerful). The wavelengths of the output photons are controlled by a tuning mirror and the crystal angle. Fast wavelength tuning (maximum 160 cm^{-1}), on a shot-to-shot basis, is possible by using piezo-electric transducers coupled to the wavelength tuning components. Longer wavelength tunings are performed by turning the components with stepper motors and thus a slower tuning response is achieved (few seconds to a minute). In the IR-mixing (infrared mixing) unit, one photon at $\lambda = 1064$ nm is mixed with an idler photon from the OPO, 730 nm $\leq \lambda \leq$ 1800 nm, to produce an output photon in the wavelength range 2600-4300 nm by difference-frequency generation. Output powers up to 100 mJ and pulse lengths of 3-4 ns are possible when using the OPO/IR-mixing units, depending on the wavelength chosen. The 355 nm laser can also be directed straight into the dome for high energy measurements (4-5 ns pulse length). The OPO and the IR-mixing unit are thoroughly discussed in [30].

The lasers are cooled by a closed-circuit water cooling system where the water temperature is controlled by compressor cooling and an electrical heater to achieve a temperature stability of ±0.5 °C. Nitrogen gas is used to create a slight over-pressure to protect the optical parts in the lasers from dust and moisture. Due to the high laser power this would otherwise result in thermal damage to the optical components [29].

3.3.2 The Dome – Part I

The manually hoisted roof-top transmission dome consists of an aluminized folding mirror (40x80 cm) situated 4 m above the ground, and can be tilted to allow the laser beam to be transmitted at different vertical angles (-10 to

55 degrees). The dome can also be rotated 360 degrees. Both rotations are done by stepper motors with a horisontal resolution of 0.0035 degrees and a vertical resolution of 0.011 degrees. This corresponds to a resolution of around 3.7x12 mm^2 at 60 m distance [29].

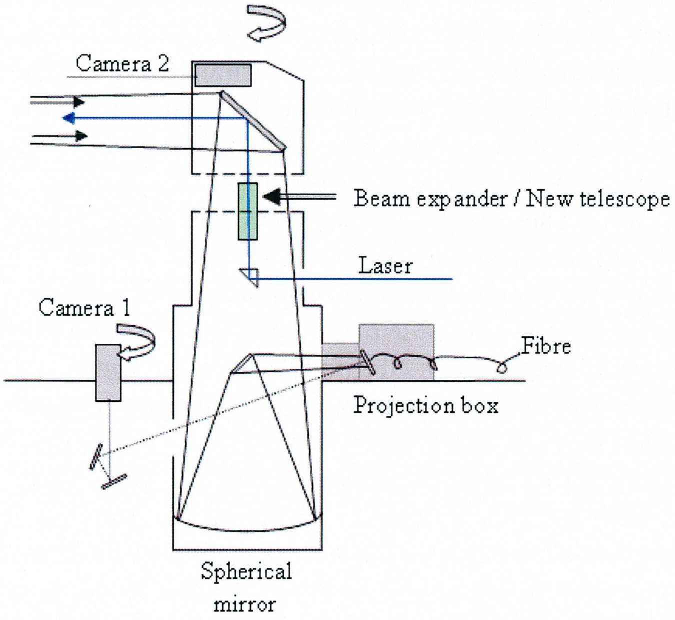

Figure 3.2: The transmission and receiving system.

A beam expander, consisting of two lenses situated in the dome above a 90 degree prism, is used to enlarge the outgoing beam (see Fig. 3.2). The first negative lens creates a divergent beam while the beam is collimated by the second lens (5 cm diameter). The reason for the magnification is to avoid causing damage to the folding mirror by a too high laser power, but also to achieve a larger laser spot on the target surface. A new beam expander was recently developed to allow LIBS measurements to be performed. The big difference between the old and this new beam expander is the larger beam profile (10 cm diameter) produced by two lenses before the light is finally focused by a third lens to create a minimum beam radius at the target surface. This is done by changing the distances between the three lenses and measuring the beam diameter at the target. The optimum dimensions of the focusing lens are determined by computer ray tracing where simulations are done (Linos Photonics, WinLens 4.3), taking both diffraction and spherical aberration into account. This yields a spot diameter of ~0.7 mm at 60 m distance. A nearly diffraction-limited beam has a Gaussian profile. If the distance to the target from the focusing lens is z, and the radius of the Gaussian beam (wavelength λ) at the lens is w, the minimum beam radius possible is given by the equation below:

$$w_0 = \frac{\lambda z}{\pi w} \tag{3.1}$$

This results in a 0.1 mm beam radius. The beam leaves the dome through a large quartz window. Due to security reasons the window has to be removed when performing LIBS measurements to avoid multiple reflections of the laser pulse which otherwise might constitute a hazard.

3.3.3 The Video Surveillance System

In order to facilitate the positioning of the laser beam, and for security reasons, a video surveillance system is incorporated into the LIDAR truck. It consists of two TV cameras, which both give a picture of the target area, and two TV monitors. One of the cameras is situated in the dome to give a large overview of the target area. The second camera is vertically mounted outside the telescope and is directed towards a couple of mirrors to be able to film a projection screen, alternatively an apertured mirror, showing the image received through the telescope.

Original System

At the onset of this project, the video surveillance system consisted of two b/w 12-inch Philips surveillance monitors and two b/w Philips TV cameras. Both the video signal and the power needed were transmitted through the same cable (75 Ohm antenna cable). The camera used for capturing an overview of the target area was equipped with a lens covering a wide angle and the camera used for filming the projector screen/mirror was using a lens covering a narrow angle range to be able to focus on the small mirror.

There were several issues with this system. Due to the need of a very light-sensitive camera for filming a projection screen (see Sect. 3.4.2), none of the old cameras could be used. There was also a wish to exchange the old b/w system for a new and up-to-date color-handling system with improved picture quality. Additionally, the system was worn from frequent use during many years, which had resulted in a slightly damaged CCD chip in one of the cameras and a damaged cable inducing interference in the video signal. Solutions to the mentioned problems are presented below.

The New System

The old system was removed and two new JVC TK-921EG color cameras (1/3" high resolution CCD: 535 TV lines, Super LoLux Sensitivity: 0.7 Lux) were installed together with two new 14 inch JVC TM-A14PN color TV monitors (320 TV lines). The new cameras have separate power and video connectors. Therefore power to the dome camera had to be taken from a power divider in the dome, also feeding a heating fan.

Figure 3.3: The new video surveillance system in action.

The old lens could be re-used with the projection screen camera, but a new lens had to be ordered for the dome camera. Finally, a minor change in the LabView code enabled the power for the cameras to be switched on and off via the computer system.

3.4 The Detection System

Here the parts of the system involved in the collection of the light radiated by the target surface are discussed (Sect. 3.4.1). A new projection box (Sect. 3.4.2) for increased security was developed. Further, the parts resolving the incoming light (Sect. 3.4.3) are discussed.

3.4.1 The Dome – Part II

The dome is used for both transmission and reception of light. The incoming light is reflected by the folding mirror at the top of the dome down to a spherical mirror situated on the truck floor. From here the light is reflected towards a mirror which directs the light into a projection box (see Fig. 3.2). The light is collected and transported to the OMA system where it is spectrally resolved. A picture taken from the inside of the LIDAR truck is presented in Fig. 3.4, where the receiving telescope, the beam expander used for transmission, the laser and the OMA system is visible.

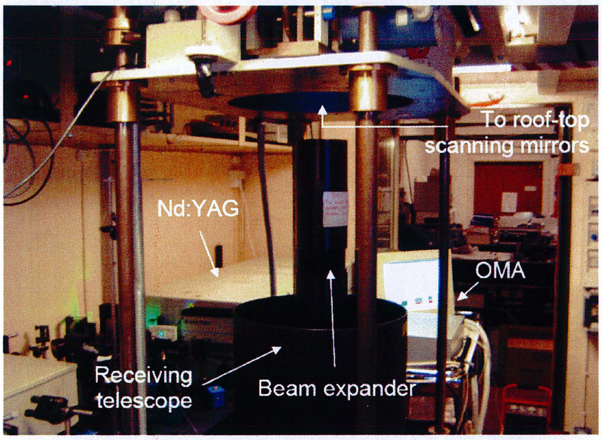

Figure 3.4: The receiving telescope and the OMA system.

3.4.2 The Projection Box

Problem Formulation

The detection box used for LIDAR and DIAL (DIfferential Absorption LIDAR) has a tilted mirror with a small hole which is placed in the focal plane of the telescope. This enables a TV camera placed on the opposite side of the dome to produce a picture of the target area, including a black spot in the center due to the aperture where light from the laser beam region passes through. This black spot is used to see where the laser beam is pointing. By rotating the camera while the dome is rotated, a non-rotating picture is seen on the TV monitor. This feature did not work properly at the onset of this project, due to a failure in the rotational mechanism.

Unfortunately, this box is not usable while performing LIF (Laser Induced

Fluorescence) or LIBS measurements. The reason is the lack of an entrance for the optical fibre connected to the OMA system, which has to be placed close to the focal plane of the telescope. Also, the absence of a fibre holder makes it unsuitable. In this case the entire box had to be removed and the fibre was positioned by a XYZ translator. A piece of paper, with a hole for the fibre tip, was mounted close to the XYZ translator to capture the telescope image but the image was too faint to shoot with the camera. Therefore there were great difficulties when positioning the beam on the target.

Among other things, the TV picture suffered from mechanical vignetting, which is an optical phenomenon that may occur in cameras where mechanical extensions to a lens protrude into its field of view (See Fig. 3.5). The result is an image with dark corners due to the obstructed incoming light [31].

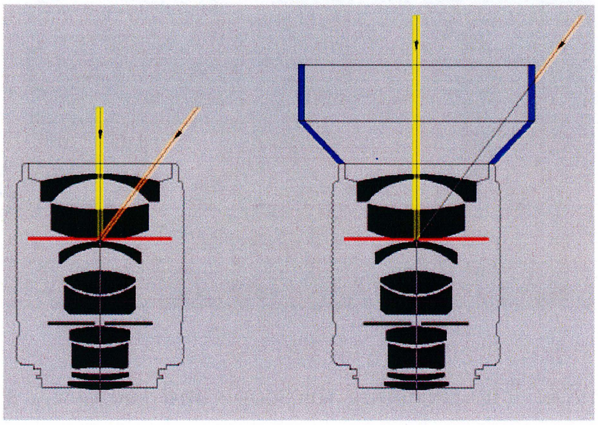

Figure 3.5: Mechanical vignetting [31]

The vignetting problem is solved by using a projection screen in the focal plane instead of a mirror and is discussed below.

New Design

The old box acted as inspiration for a new detection box based on projection. The dimensions of the box are 280x160x195 mm^3. The entry of the projection box, towards the telescope, is shielded to avoid light from lamps and other light sources to reach the projection screen. The only light allowed is the light that has been reflected by the spherical mirror and then directed into the box, or in other words: the light from the target surface. A filter is placed in front of the projection screen to block resonance radiation, Rayleigh scattered light and surface reflected light at the laser frequency. On the backside of the box there is a hole for the optical fibre.

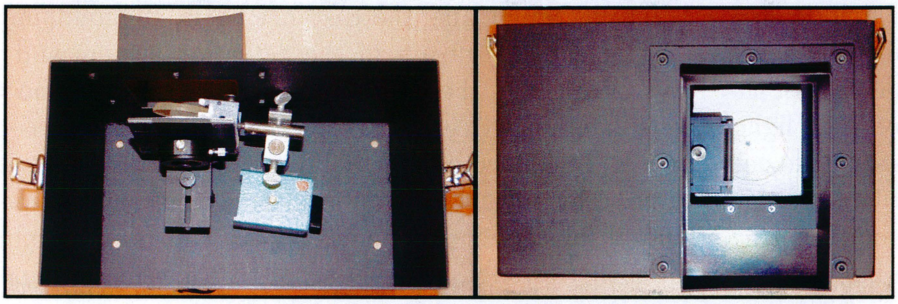

Figure 3.6: The new projection box

The projection screen is a tilted metal surface, with a small hole in the center, attached to a metal plate which can be moved back and forth or be rotated on a frame. A white projection cloth, especially manufactured for projection purposes (home cinemas), is attached to the projection surface with adhesive tape. The projection surface is placed so that the small hole is situated in the focal plane of the telescope. In this way the optical fibre can be positioned with its tip very close to the focal plane, to be able to collect all laser-induced light.

Due to the large amounts of light needed to achieve a clear picture, the projection feature of the box can only be used at day-time measurements. Night-time measurements can still be performed with the box mounted to the telescope, but with decreased security and difficulties to position the beam on the target surface.

Finally, the rotational mechanism of the rotating camera was repaired and adjusted to fit the new colour TV camera.

3.4.3 The Optical Multichannel Analyser

The optical multichannel analyser (OMA) is a time-gated image intensified light detector. The incoming light, via the optical fibre (600 μm diameter), is dispersed by a spectrometer (Oriel Corporation MS125), consisting of a reflection grating (400 lines/mm), and is projected onto an Andor DH50125U-01 Charged Coupled Device (CCD). The CCD has 1024 channels where the light is converted into an electric signal. A current proportional to the channel intensity is sent to a computer for evaluation. A delay generator is connected to the detector to be able to choose when the detection shall start after the laser pulse has been released from the laser cavity. Depending on the time dependence of the radiating target and the distance to it, different delays have to be chosen. Due to internal delays in the detection system and the signal cables, the delay value set in the delay generator differs from the real delay. The light travels 2x60 m (twice the distance to the target areas discussed in the next chapter) in 400 ns, but the delay must sometimes be set to a much lower time value. This means that only relative time measurements can be performed if no absolute starting point, $t = 0$, can be determined. The built-in image intensifier strengthens the signal to allow measurements of low light intensities. By only measuring in a short time interval, for instance only when the incoming laser-induced signal is strong, the otherwise dominating background light is suppressed [32].

3.5 Software Development

Soon after the measurements had begun, we noticed that a quick and reliable program was needed to identify peaks in the collected spectra. The program should also be able to handle a database with elemental data for swift suggestions on which elements the peaks belong to. The software, developed in Microsoft Visual Basic 6, is called *PowerSpectrum* and gradually grew into a well-working companion. The reason for choosing Visual Basic as programming language instead of LabView, otherwise used in the mobile lidar system, is the author‘s familiarity with Windows programming and the need of a fully working program in a couple of days. It was not possible to learn a whole new programming language in such a short time.

3.5.1 Calibration

The OMA system was calibrated with the help of a helium lamp for detection of narrow isolated peaks, and a first-order polynomial was adapted to allow translation between channel number and wavelength. While running PowerSpectrum we noticed that this simple built-in interpolation routine (constructed by Ref. [32]) had insufficient accuracy. The solution was to implement a separate calibration routine in PowerSpectrum which could handle an arbitrary polynomial order. This was done by implementing matrix operations like Gauss elimination, transpositioning and multiplication to achieve inverted matrices, etc. for use in a routine based on the Least Squares Method. The polynomial coefficients ($\mathbf{c}$ vector) are calculated by the use of

Eq. 3.2, where $\mathbf{x}$ contains the channels, $\mathbf{y}$ contains the wavelengths and $\mathbf{A}$ is a m x n matrix with the contents according to Eq. 3.3.

$$\mathbf{c} = (\mathbf{A}^T\mathbf{A})^{-1}\mathbf{A}^T\mathbf{y} \tag{3.2}$$

$$\mathbf{A} = \begin{pmatrix} 1 & x(1) & x(1)^2 & \ldots & x(1)^{n-1} \\ 1 & x(2) & x(2)^2 & \ldots & x(2)^{n-1} \\ 1 & x(3) & x(3)^2 & \ldots & x(3)^{n-1} \\ \vdots & \vdots & \vdots & \ddots & \vdots \\ 1 & x(m)^1 & x(m)^2 & \ldots & x(m)^{n-1} \end{pmatrix} \tag{3.3}$$

Second-order interpolation was found to be most efficient due to the analytical solutions of the second-order equation needed when translating wavelength into channel number (followed by a conversion from channel number to a screen coordinate). The accuracy increased dramatically in comparison to the use of a first-order polynomial. The reason for the non-linear behaviour of the OMA might be a slightly bent grating or other not optimum-shaped components (CCD, mirrors, lenses, etc).

When using polynomial orders > 2, the solutions to the equation

$$f(x) = c_n * x^n + c_{n-1} * x^{n-1} + \ldots + c_1 * x + c_0 - \lambda = 0, \tag{3.4}$$

where x is the channel number and where the wavelength λ is given, have to be computed by iterating methods like the Newton-Raphson method. A start value, x_0, is set to the shown mid channel number and iterations are done according to

$$x_n = x_{n-1} - \frac{f(x_{n-1})}{f'(x_{n-1})}, \qquad n = 1, 2, \ldots \tag{3.5}$$

until $|f(x_n)|$ is less than a bailout value statically set in the program (10^{-5}). The output of the method is x_n = the translated channel. The use of the simple starting point guessing function above is justified due to the, expected, strictly increasing behaviour of the wavelength function. Normally, in the case of Newton-Raphson iteration, a start value must be cleverly guessed close to the correct one to ensure convergence towards the real root.

Higher order interpolation, $2 < n <$ *marked peaks*, resulted in an even better accuracy of the translation routine. However, the resolution of the OMA system is ≈2.2 nm, which gives a large uncertainty of the peak positions set manually in the program when calibrating, which is much larger than the interpolation error. Interpolating at an equal or higher order than the number of marked peaks resulted in large deviations due to the fact that the calculated polynomial is not unique.

The emission spectral lamp used for calibration can be freely chosen and by manually marking the peaks in the spectrum the program automatically calculates the coefficients in Eq. 3.4.

3.5.2 Identification

Several strong elemental lines [33] were added to a database file and loaded into the program. By clicking with the mouse pointer on a peak in the spectrum, the program suggests which element it may belong to together with the deviation compared to the database entry. This is, however, not the quickest way to identify the target material. A feature was implemented where the user can choose an element and let the program show vertical coloured identification lines in the spectrum. In this way several peaks can be identified with one mouse-click. The desired ionisation grade of the element of interest can easily be chosen. A screen-shot from of the program while identifying He lines is show in Fig. 3.7.

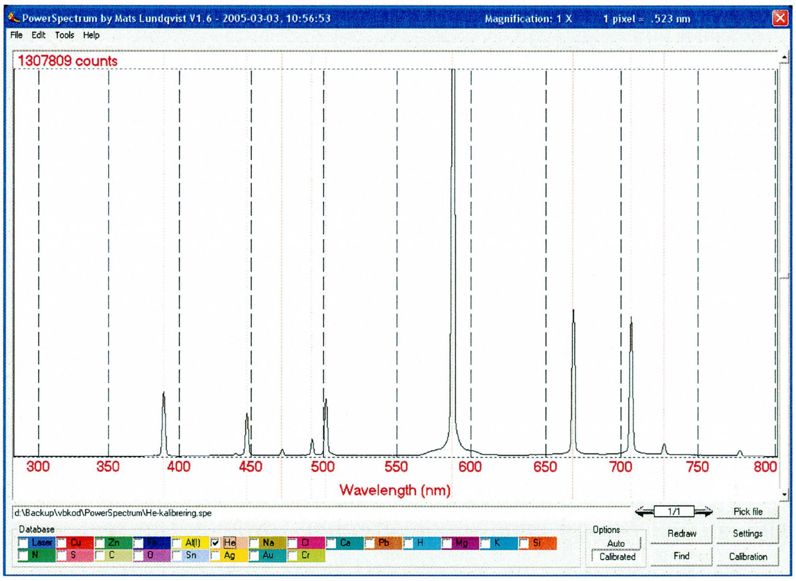

Figure 3.7: Identification of helium peaks after second-order calibration of the wavelength scale.

Other features implemented:

- A warning system which is activated when trying to identify peaks situtated at wavelengths longer than the double laser wavelength. This measure of precaution is taken because the peak may be a second-order reflection of the grating in the OMA. When clicking with the mouse pointer on such a peak at λ, an arrow pointing at a possible peak at the spectrum position $\lambda/2$ is drawn. If no peak is situated at $\lambda/2$, the conclusion can be drawn that this really is a "real" peak.
- Zoom feature.
- Find-button which scans the spectrum to find peaks and automatically identifies them. This feature suffers from low accuracy due to the simple peak-identification routine. A threshold can be chosen to only allow, for instance, strong peaks to be identified.
- Ability to save spectra for presentation purposes.
- A Fast Fourier-Transform routine, which has no direct use at the moment, but could be adapted to filter the spectrum for improved identification.
- Auto-button which forces the program to load the latest saved spectrum file into the memory.
- Unsensitivity to screen resolution. This means that any screen resolution can be used and still the program makes the best use of the available screen space.
- A debug feature for easy error recognition.

Chapter 4

Measurements

4.1 Introduction

Remote LIBS measurements on metals, stones and crystals have been performed, both point and imaging measurements, and are presented in Sect. 4.2. Also, remote ablative cleaning of an Italian garden statue (replica) and an Italian replica statue head made of marble has been performed and is presented in Sect. 4.3. Finally, a discussion about how future remote Raman measurements could be executed is included in Sect. 4.4.

4.2 Remote LIBS

Earlier tests [30, 34] suggested that Remote LIBS at a distance of 60 m could be practicable with the LIDAR truck. These measurements were performed with the old beam expander and a remote focusing lens (f=50 cm) positioned in front of the target surface. The collected spectra from aluminium and other metals contained several strong and identifiable peaks. Still, there was an uncertainty if the system really could perform "real" Remote LIBS measurements with a different beam expander and without a remotely positioned lens. The influence of the latter on the backscattered light from the target surface cannot be neglected and may dramatically improve the collected signal due to the increased solid angle collected by the folding mirror.

4.2.1 Setup

The distance from the LIDAR truck to the target area was around 60 meters, determined in earlier measurements by changing the delay to the detector. A frequency-tripled Q-switched Nd:YAG laser emitting at 355 nm was used. To achieve a perfectly vertical beam in the telescope and the beam expander, avoiding distortion of the beam shape, the laser beam had to be aligned. The entrance hole in the telescope for the laser beam was situated at a different height above the truck floor compared to the output plane of the laser which complicated the alignment. Despite a good alignment the beam shape still suffered from astigmatism implying that the beam expander lenses are not perfectly mounted or cut/polished.

The black spot on the TV monitor used for guiding the laser beam to the target area was large and the optical fibre had to be manually aligned by translation of the fibre tip in a XY translator. To find the optimum fibre position, a white paper sheet was held in front of the target surface while transmitting a laser beam with a large (~5 cm) beam radius (to avoid creating breakdown) inducing strong fluorescence light. The position of the fibre tip was then changed until a maximized signal was detected by the OMA.

The average laser power was increased to an estimated limit of 3.0-3.4 W (150-170 mJ/pulse at 20 Hz repetition rate) to avoid damaging the folding mirror. Pulse energies up to 35 mJ were considered safe to transmit with the old beam expander. Due to the twice as large beam diameter produced in the new beam expander, the beam is covering a four times larger area on the mirror surface. Thus, four times higher pulse energy can now be transmitted. By changing the position of the lenses in the beam expander, the beam focus could be positioned at the target surface and a minimum beam radius could be achieved. The beam diameter at the target surface was measured to be around 5 mm which results in a power density of $1.5\text{-}1.7 \cdot 10^8$ W/cm^2. This value is very close to the suggested lower limit for LIBS action (see Sect. 2.4.2). While doing some measurements it was observed that laser sparks were sometimes randomly created in the whole area of the laser spot due to "hot spots". Before a measurement could be performed, a background spectrum had to be collected with the OMA system which was later subtracted from the collected spectra. Due to varying sun light intensities at the different targets, background calibration had to be performed frequently.

4.2.2 Point Measurements

Different stones and minerals (pyrite, granite etc) were collected at the coastal line close to Simrishamn in southern Sweden to be examined by Remote LIBS. In an old silver mine called “Impan“ near Gladsax, where silver was extracted from 1562 until 1760 and aluminium in the 20th century, numerous interesting minerals were found too. Also building materials (Siporex, mortar, alabaster and marble) and other substances, including metal plates mounted on a target holder, were examined. Point measurements on the above mentioned materials have been performed and are further discussed below. The view of the target area from the truck is shown in Fig. 4.1. The starting point, $t = 0$, was determined by incrementally increasing (50 ns steps) the delay value set in the delay generator from 50 ns to 2000 ns, while collecting spectra from lead. A short 50 ns gate was used. The measurement using a 100 ns delay showed the onset of a tiny peak at 355 nm, indicating that the earliest returning light was detected around 150 ns. This was verified in the next measurement using a 150 ns delay, where a very strong peak was seen in the spectrum. By subtracting 150 ns from all set delays, an approximate absolute time scale was achieved.

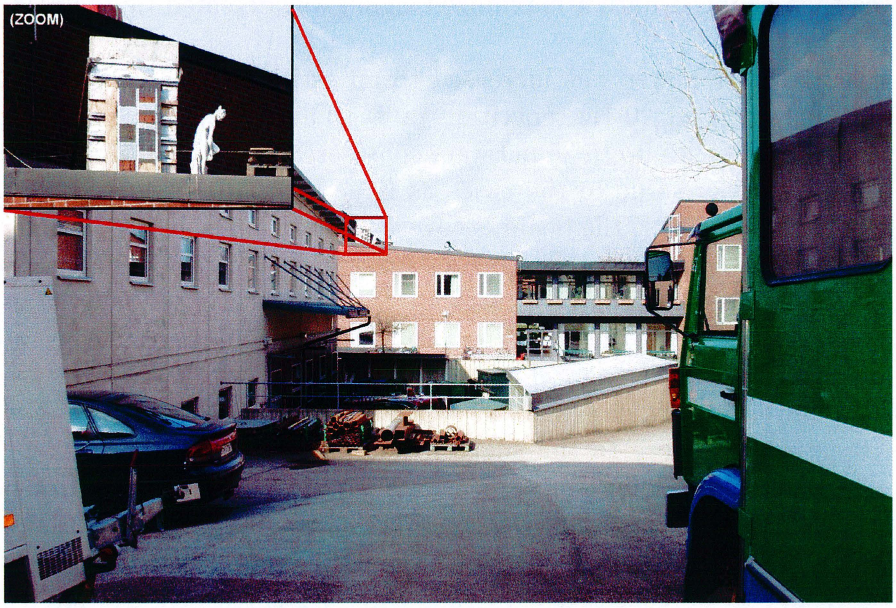

Figure 4.1: The view from outside the LIDAR truck while performing point measurements, in the direction towards the target area.

Metals

The metal at the top of Fig. 4.2 is pure copper (Cu). The delay was set to 250 ns and a 150 ns gate was used, resulting in a time window around 100-250 ns for the detection. The pulse energy was 170 mJ and the integrated spectrum was constructed from measurements of 500 pulses. Strong emission peaks from neutral copper atoms can be seen in the visible region of the spectrum. No peaks originating from copper ions can be identified. The action of a color filter in the OMA system blocking light around 400 nm is clearly seen in the spectrum and in some of the upcoming spectra. The sodium 589 nm doublet peak is observed in the spectrum due to a contamination of the copper sample. In the middle of Fig. 4.2, a spectrum from brass is presented ($350 \leq t \leq 450$ ns, 200 pulses with 150 mJ/pulse). Brass is an alloy containing both copper and zinc atoms (63% Cu and 37% Zn) and, in addition to the copper peaks also shown in the previous spectrum, three peaks from neutral zinc and one peak from singly-ionised zinc are visible (despite the long delay). The spectrum from the iron (Fe) plate, situated at the bottom of Fig. 4.2, contains many strong peaks in the wavelength range 400−550 nm ($150 \leq t \leq 250$ ns, 200 pulses with 150 mJ/pulse). The cleaning effect of the focused beam is clearly seen in the small photograph of the oxide-covered iron surface (the grey areas).

Hardened aluminium, called duraluminium (top of Fig. 4.3), is an alloy containing aluminium and magnesium. Two strong magnesium peaks are visible on both sides of the aluminium peak in the spectrum ($100 \leq t \leq 250$ ns, 500 pulses with 170 mJ/pulse). Breakdown was easily achieved in duraluminium, but in normal aluminium only a very noisy signal was collected – still good enough to see the strongest peak. The metal plate in the middle of Fig. 4.3 is made of stainless steel which contains both iron and chromium. Two very strong chromium peaks are seen in the collected spectrum ($0 \leq t \leq 100$ ns, 200 pulses with 150 mJ/pulse) among the strong iron lines. Due to the short delay, the light from the strong plasma continuum is still visible in the spectrum. Nevertheless, the peaks are easily identifiable. Finally, lead (Pb) was examined and the collected spectrum ($100 \leq t \leq 250$ ns, 500 pulses with 170 mJ/pulse) is presented at the bottom of Fig. 4.3. Optical breakdown was easily achieved with strikingly loud sound bangs. According to Ref. [33] the peak at 723 nm should be almost equally strong as a the peak situated at 375 nm (second peak from the left). This indicates that the detector sensitivity is decreasing close to 800 nm. Possibly, a peak from sulphur ions (S^+) is also be visible in the spectrum.

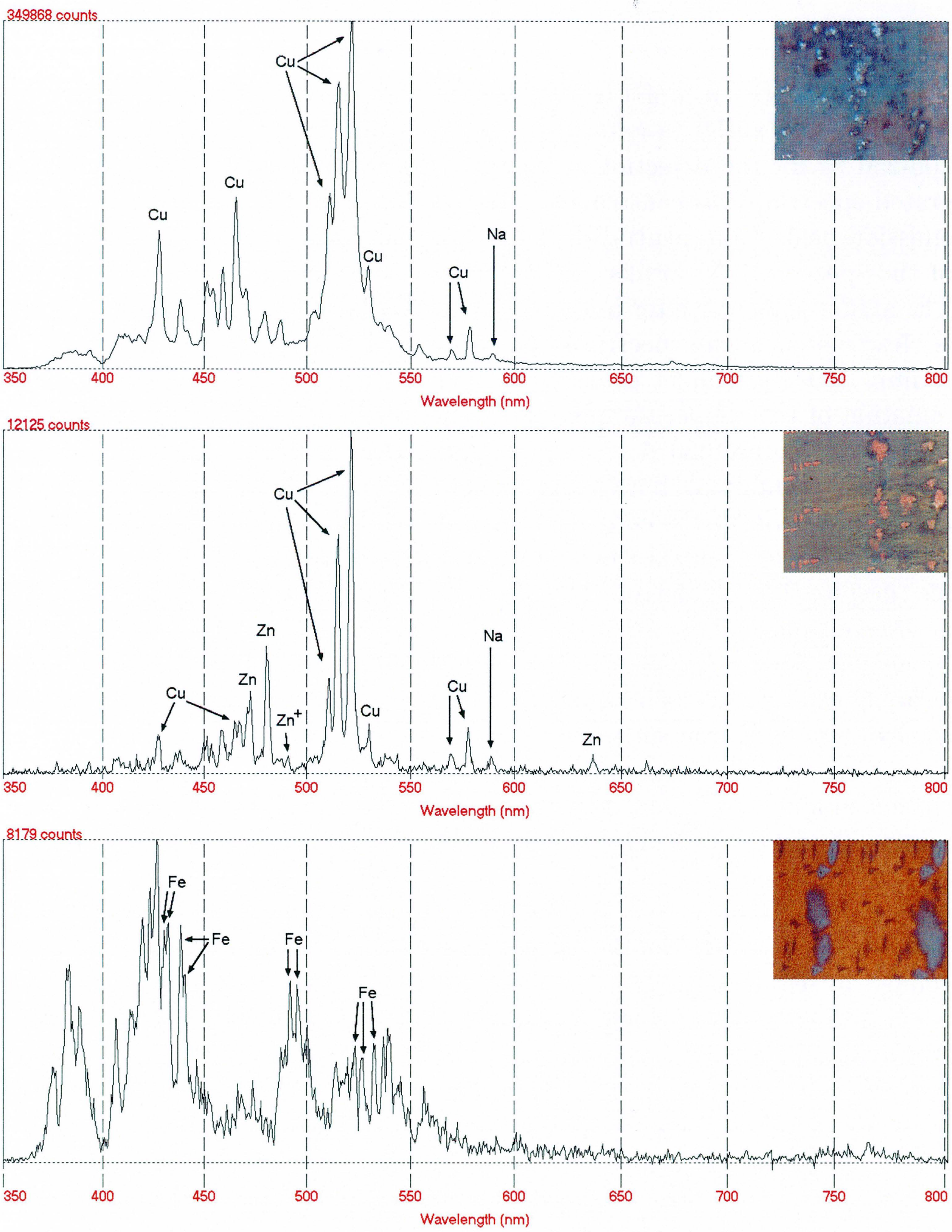

Figure 4.2: LIBS spectra from copper (top), brass (middle) and iron (bottom).

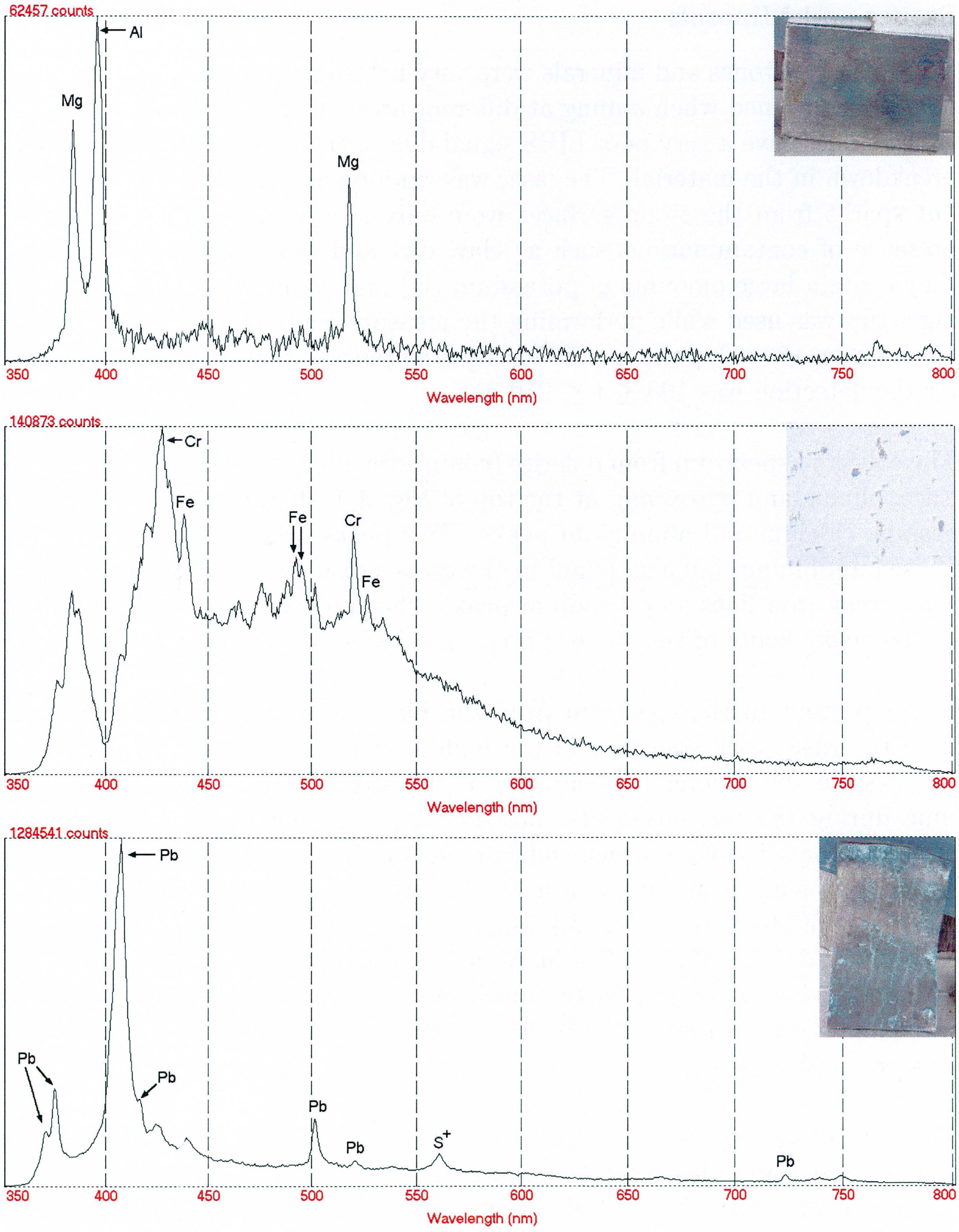

Figure 4.3: LIBS spectra from duraluminium (top), stainless steel (middle) and lead (bottom).

Stones and Minerals

The collected stones and minerals were very heterogeneous and different signals were obtained when aiming at different areas of the same object. Many of the stones gave a very poor LIBS signal due to the failure to create optical breakdown in the material. The laser was running at a 20 Hz repetition rate but sparks from the stone surfaces were only seen occasionally. Also, the presence of contaminations such as clay, dirt and salt could be verified as they contain large amounts of potassium (K) and sodium (Na). The following setup was used while performing the measurements below: 250 ns delay, 150 ns gate, 170 mJ/pulse and 500 integrated pulses. Thus, the time window for the detection was $100 \leq t \leq 250$ ns.

The collected spectrum from dolerite (composite mineral consisting of plagioclase, olivine and pyroxene), at the top of Fig. 4.4, shows some strong magnesium, calcium and aluminium peaks. Two peaks originating from singly-ionised aluminium are also found in the quite noisy spectrum together with some weak iron lines and a sodium peak. The spectrum is a good example of how noisy many of the stone spectra, not included in this thesis, were.

In comparison to the spectrum from the black stone above, the spectrum from the rusty rock (biotite), in the middle of Fig. 4.4, looks quite identical, despite the different appearance of the stone. For the first and only time during the measurements, possibly a peak from double-ionised aluminium atoms is found which indicates a high plasma temperature. Also strong potassium peaks are seen in the interval 766 − 770 nm despite the low sensitivity of the detector in this range. The chemical formula of biotite is $K(Mg,Fe)_3AlSi_3O_{10}(OH)_2$. The rusty surface indicates a large content of iron hydroxide which is proved by the much more conspicuous iron peaks in the spectrum. Two burn-marks from the measurements on the stone surface can be seen.

The last spectrum was collected from calcite ($CaCO_3$), contaminated by quartz (SiO_2) and clay minerals (containing some aluminium), and is seen at the bottom of Fig. 4.4. Peaks from both neutral and singly-ionised aluminium atoms and calcium atoms can be seen in the spectrum. The calcium and aluminium peaks overlap slightly which makes it difficult to identify the peaks. By carefully comparing with other spectra containing either only calcium peaks or aluminium peaks, it is possible to draw the conclusion that both elements must be present in the current spectrum due to the very broad lines. Additionally, very weak silicon peaks can be found.

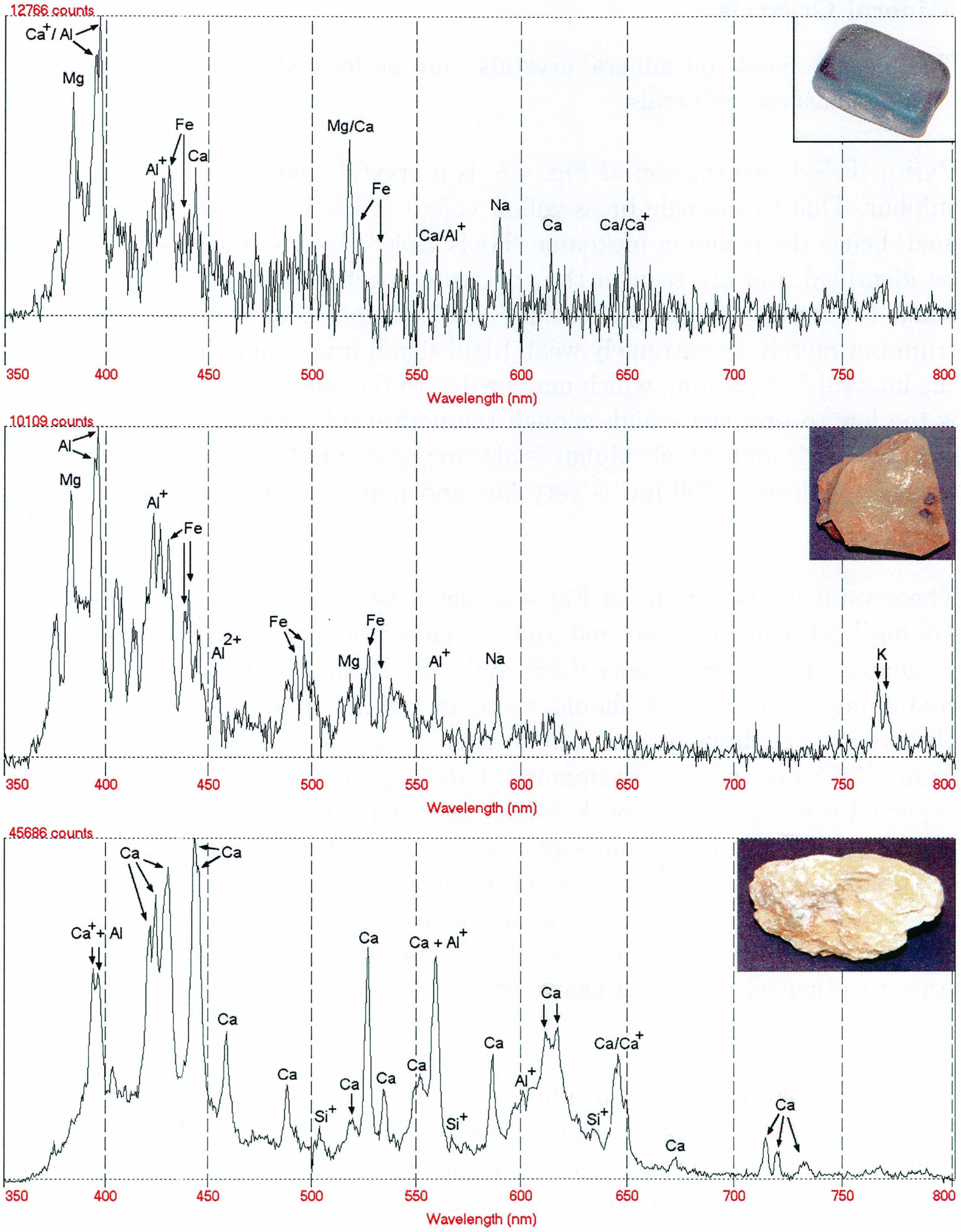

Figure 4.4: LIBS spectra from dolerite (top), biotite covered by iron hydroxide (middle) and calcite/quartz/clay minerals (bottom).

Mineral Crystals

The measurements on mineral crystals were performed with the same setup as the stones and minerals.

Pyrite (FeS_2), see the top of Fig. 4.5, is a crystal containing both iron and sulphur. Due to the pale brass-yellow colour it has often been mistaken for gold, hence the common nickname "Fools Gold". Very strong iron peaks can be identified and are seen in the spectrum together with a weaker sodium peak. No strong and easily identifiable sulphur peaks are found in the spectrum but merely an extremely weak LIBS signal from singly-ionised atoms in the interval 545-560 nm, which may be due to the fact that the power density is too low to produce a high enough temperature for effective ionisation. A strong peak from neutral sulphur is also expected at 792 nm but the detector sensitivity close to 800 nm is very low and may explain the absence of the peak.

The crystal in the middle of Fig. 4.5, has a very interesting spectrum containing both calcium, lead and zinc. Conceivable components of the inhomogenous crystal are Galena [PbS] and Zinc Blende [(Zn,Fe^{2+})S] [35], both containing sulphur which should result in visible sulphur peaks due to the observed strong breakdown. In fact, there is a broad strong peak from calcium (559.5 nm) with a maximum situated approx. 1 nm to the left of the expected position of a S^+ peak (560.6 nm). A possibility is that the sulphur peak is hidden in the calcium signal or even, due the small distance between the theoretical peak positions, is contributing to the peak width. Also, faint peaks are visible close to the calcium peak, strengthening the assumption that sulphur is present. A very weak sodium signal can be seen in the spectrum together with calcium peaks originating from the calcite rock which is mixed into the crystal.

The purple crystal at the bottom of Fig. 4.5 is called Fluorite (CaF_2) and can be found in many other colours (white, yellow, green, red, blue and even colourless). The structure of the crystals is mostly cubic which facilitates the identification. The collected spectrum contains no sharp emission peaks which are characteristic for a normal LIBS signal. Instead, a very broad fluorescence peak is seen, suggesting that no optical breakdown was created in the crystal. In some cases the crystals, like quartz (SiO_2), were totally transparent to the laser light and breakdown was only achieved in the lower-lying mineral. When these crystals were growing on substrates like calcite, only noise or a very weak fluorescence continuum was collected.

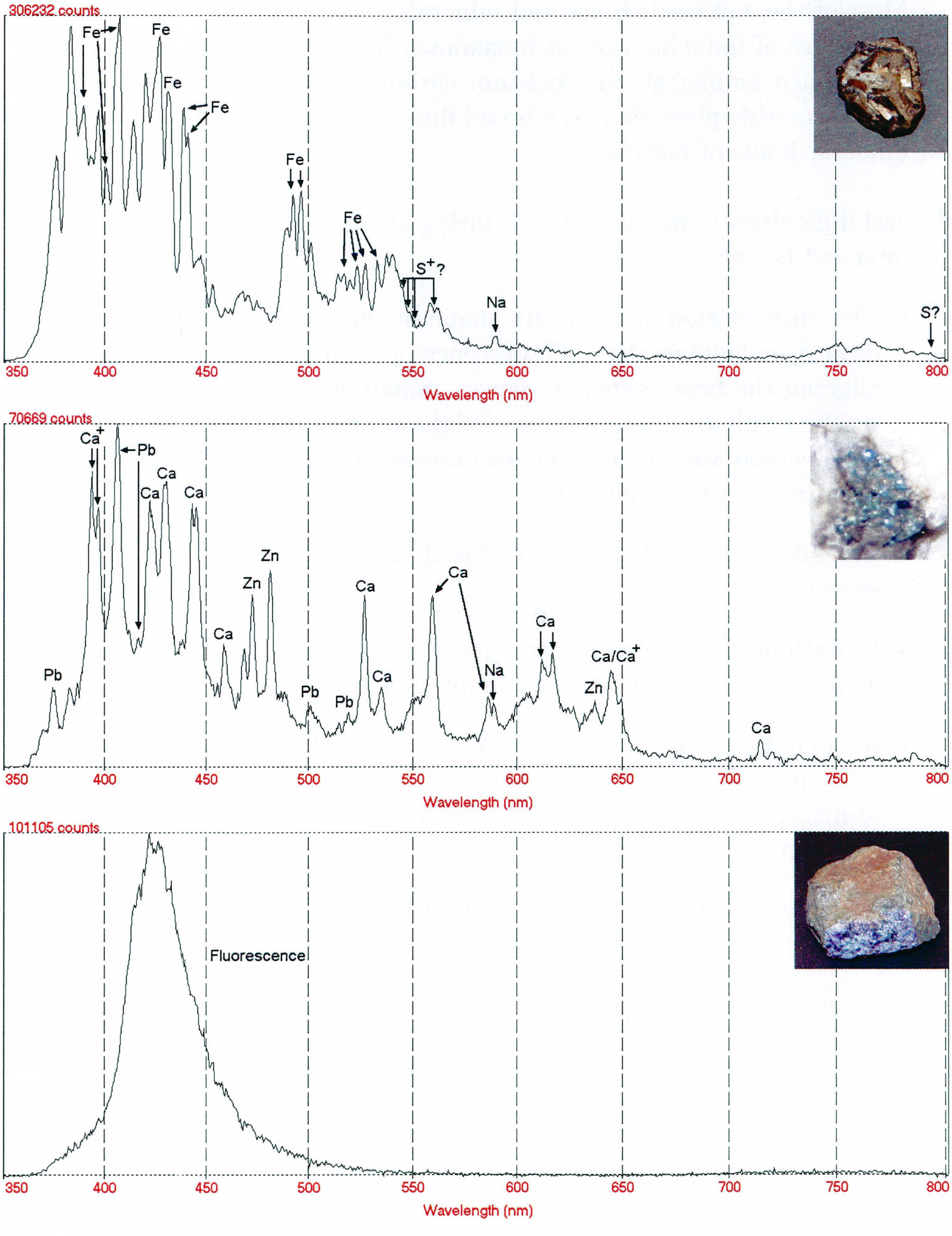

Figure 4.5: LIBS spectra from pyrite (top), galena/zinc blende (middle) and calcium fluoride (bottom).

Most of the collected stones and minerals gave no LIBS signal at all due to the failure of inducing optical breakdown in the material. This was also the case when aiming at pure calcium carbonate, Siporex, mortar and alabaster. A marble piece showed a broad fluorescence spectrum characteristic for different kinds of marble.

Several difficulties were encountered during the measurements and these are summarized below:

- The optimization of the beam shape in the focal point had to be performed by looking at the fluorescence light from a piece of paper while aligning the beam expander lenses. Small adjustments of the lens positions resulted in large changes of the beam properties. The optimum beam shape was found to be oval due to the astigmatism of the lenses resulting in a lower efficiency.
- Breakdown was achieved in different points of the beam profile (hot spots).
- Vibrations of the LIDAR truck (movement in truck results in movement of ablation point) in spite of the lowered hydraulic support legs.
- It was not possible to create breakdown in all of the examined materials. More pulse energy would create a higher power density on the target resulting in a higher success rate, but the dome mirror might not handle higher pulse energies.
- The materials had to be nearly flat-surfaced and preferrably perpendicular to the beam direction to create optical breakdown most efficiently.
- Many elements have strong peaks in wavelength areas where the OMA system does not work (below 350 nm or above 800 nm).
- Second-order diffraction peaks from the grating in the OMA system increases the risk of false peak identification.
- Line-broadening mechanisms affect the collected signal. Also, slight shifts of the peak positions make elemental identification difficult.
- Noisy signals due to the absence of breakdown in every laser shot.

Time Evolution

Six measurements were performed to investigate the time evolution of copper LIBS spectra (See Fig. 4.6). A 100 ns gate and delays in the interval 150 to 800 ns (covering the time interval $0 \leq t \leq 750$ ns) were used during the measurements. In the first spectrum (a), recorded at $0 \leq t \leq 100$ ns, a broad plasma continuum is seen with line-broadened discrete emission peaks superimposed. At $50 \leq t \leq 150$ ns (b) the plasma glowing is decreasing and the emission peaks are becoming narrower until $100 \leq t \leq 200$ ns (c) where the plasma continuum has almost disappeared. The three strongest copper peaks are not fully separated; still this is the optimum delay for identification of the peaks since all peaks are strong. At $150 \leq t \leq 250$ ns (d) some of the peaks start to decrease in strength and width which separates them even further. This is clearly seen after 350 ns (e) and 650 ns (f).

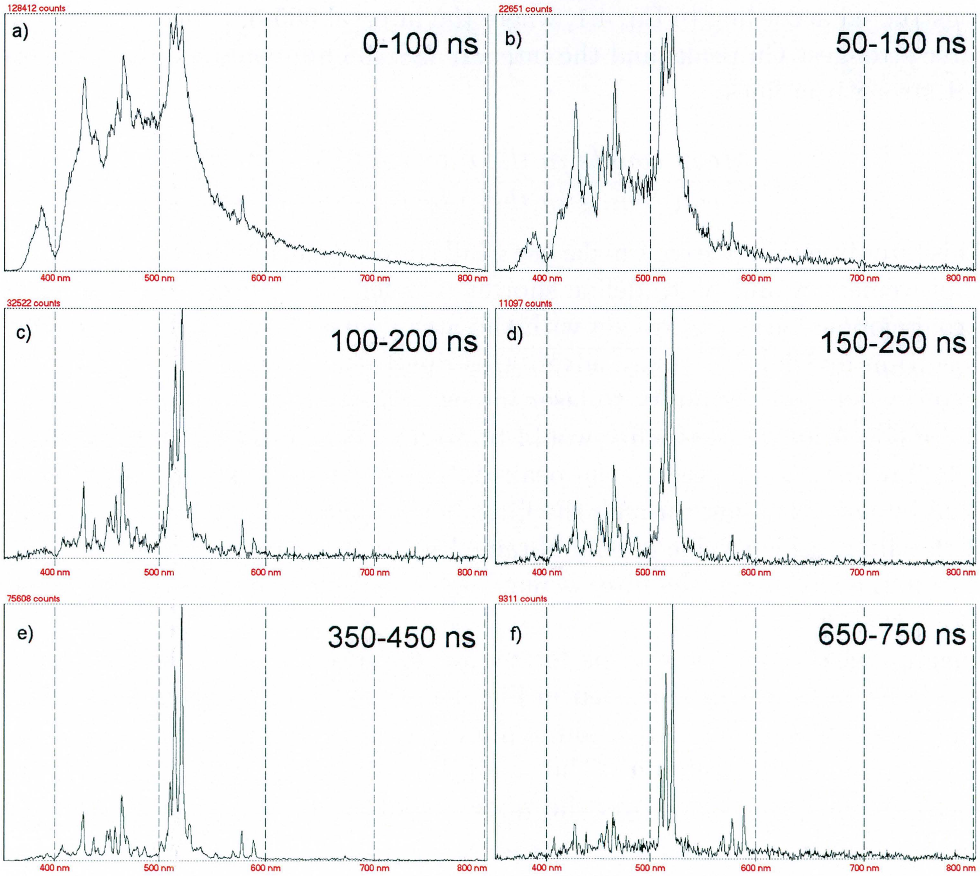

Figure 4.6: Time evolution of copper spectrum

4.2.3 Imaging Measurements

By sweeping the focused laser beam over a target area under computer control, and collecting an integrated spectrum in each point, it was possible to produce LIBS images. This technique is called Remote Imaging LIBS and was, to our belief, performed for the first time. The images were constructed by evaluating a filter function, where intervals covering the widths of some strong peaks belonging to a certain element were manually selected in a LabView program. Also some areas with very low peak intensity were selected, preferably where other elements than those expected to be detected have strong peaks. In every image point the spectra are compared in these manually selected intervals and the output value of the filter function is large if a spectrum contains peaks at the selected positions and low if it does not.

As an example, the filter function for classifying spectra containing copper is constructed according to Eq. 4.1, where the interval 505-527 nm contains the three strongest Cu peaks and the interval 488-498 nm contains no Cu peaks but strong iron lines.

$$f = \frac{Mean\ counts\ in\ the\ interval\ 505 - 527\ nm}{Mean\ counts\ in\ the\ interval\ 488 - 498\ nm} \tag{4.1}$$

This filter function does not make use of all copper peaks in the spectrum. An improvement would be to define shorter wavelength intervals covering each strong copper peak and divide with the areas outside the marked intervals. Spectrum division has many advantages due to the resulting dimensionless quantity, such as immunity to laser intensity fluctuations and angle of incidence [2]. Another possibility would be to use correlation techniques where a digital filter is adapted to the peaks in the spectrum. By subtracting the total intensity passing through the filter before and after a small translation of the filter, a high value is only obtained if the intensity difference is large. This is the case when the filter is matching the sought for spectral peaks.

Imaging measurements were performed on an arrangement of metal plates. The large metal plates to the left in Fig. 4.7 are made of (starting at the top) copper, stainless steel, brass, aluminium and iron. Stainless steel contains besides iron some chromium. The smaller plates on the right hand side are identified below. A sweep over the whole metal target area at 60 m distance was performed (6x21 points) and is presented in the right part of Fig. 4.7.

This figure was produced manually by saving a false-coloured picture for each element in different colors and combining them to a single picture. Image

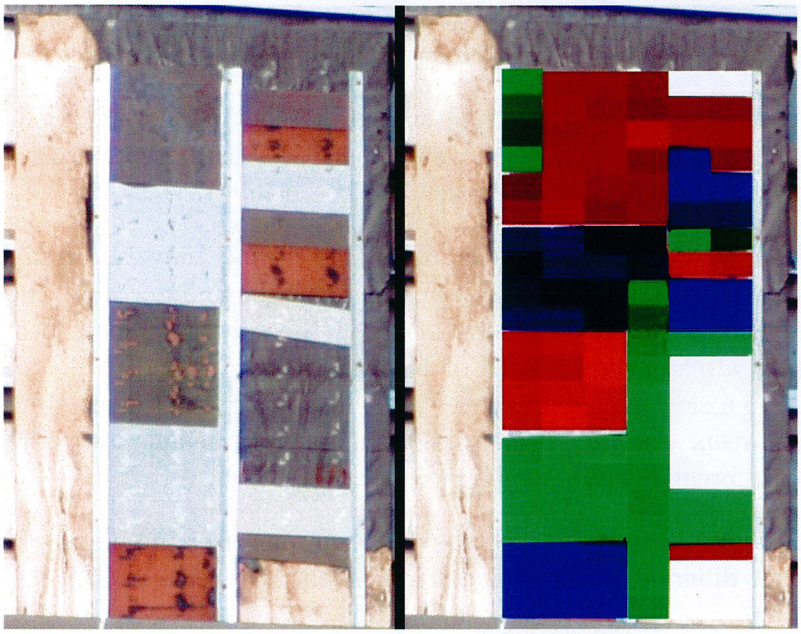

Figure 4.7: Remote Imaging LIBS – Cu (red), Al (green) and Fe (blue)

points coloured red contain copper atoms and the plates made of copper and brass are imaged in perfect agreement with the previous description of the metal plates. Additionally, three small metal plates to the right are classified as copper atom carriers. The stronger copper signal from brass compared to pure copper implies that breakdown might be easier to accomplish in brass. Another reason can be a slightly different time dependence.

Green image points contain aluminium atoms and the aluminium plate on the left side is correctly imaged. Three small aluminium plates are also found. Due to the tilted setup of the metal plate targets, the laser beam occasionally hits the vertical profiles holding the plates. The result is an additional occurrence of green image points.

Finally, blue image points show areas containing iron. The big metal plate at the bottom of Fig. 4.7 is as expected identified as iron and so are also two smaller plates to the right. The dark blue pixels belonging to one big and one small stainless steel plate are also seen due to the presence of iron. White areas in the figure are non-metallic surfaces (wood and paper).

There are some additional difficulties arising when performing Remote Imaging LIBS in comparison to point measurements:

- Material points may be situated at different distances from the dome mirror, resulting in varying power densities at different target surfaces due to the non-optimum position of the beam focus.
- Elements have different time dependence and may result in the detection of some elements while other remain undetectable due to the absence of the characteristic peaks in the spectra. These peaks have either already disappeared or have not yet appeared in the spectrum due to a slow time dependence and the statically set delay time during the sweep. Another reason might be an unsufficient power density to create breakdown in some materials.
- Sun-light affected the spectra while scanning over the metal plates due to the different angles of incidence on the plates.

4.3 Remote Ablative Cleaning

Remote Ablative Cleaning is a method to clean surfaces at large distances. The procedure is either self-terminating when hitting the original surface or guided by spectroscopic control. Remote cleaning of an Italian garden statue (replica) at 60 m distance, covered by dirt and algal growth, was successfully performed and is presented in Fig. 4.8. The picture to the left (a) shows a thigh belonging to the statue and was taken before any cleaning had been done. The pollution layer can clearly be seen. The picture in the middle (b) shows a surface cleaned by sweeping the laser beam row by row over the surface (6x6 points). An improved cleaning efficiency in the left part of the ablated area is evident. This is due to mechanical backlash in the gears

Figure 4.8: Remote Ablative Cleaning

operated by the stepper motor causing the laser beam to stop for a while after returning to the left-most scanning point. Furthermore, the cleaned area looks quite striped due to large scanning steps. The picture to the right (c) shows a clean area with only very faint stripes. These stripes would have disappeared if the cleaning procedure had taken a longer time. The laser beam was then programmed to only stop in the outermost points of the area to be cleaned. This ensured that the laser light was evenly spread and a more efficient cleaning procedure was obtained. An area of an Italian replica statue head made of white Carrara marble was blackended by a soft pencil before remote cleaning was performed. In the left picture (a) of Fig. 4.9 the painted area can be seen. The right picture shows the same area after the cleaning had been performed, resulting in a clean surface in good condition.

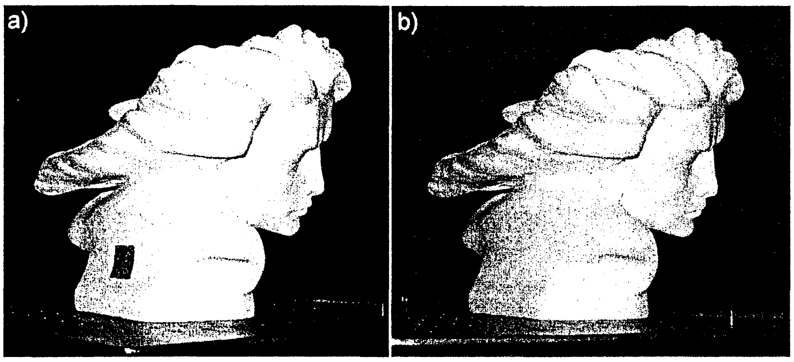

Figure 4.9: Remote Ablative Cleaning

In addition, successful cleaning of alabaster and mortar was also performed. By using a tighter focus, green copper oxide was removed from a copper plate while looking at the resulting LIBS spectrum (spectroscopic guidance). The spectrum changed dramatically when the clean surface was reached, showing strong Cu peaks in contrast to the very noisy spectrum collected from the copper oxide covered parts. The measurements have resulted in an article included in Appendix A, which has been submitted to Optics Letters. Also, a conference contribution is included in Appendix B.

4.4 Raman Spectroscopy

Before performing remote Raman measurements a compromise has to be made in the choice of laser wavelength, considering the decrease in Raman line-strength at longer wavelengths ($\propto \lambda^{-4}$), the suppression of fluorescence light at longer wavelengths and the proper selection of filters blocking the Rayleigh scattered light. In addition, the choice of a suitable detector has to be made, with a high enough resolution to resolve the close-lying narrow Raman peaks and with high sensitivity in the wavelength range where the peaks are positioned. Another advantage when using a long laser wavelength is the increased separation between two Raman-shifted peaks, such as the Stokes-shifted calcium carbonate line at 1007 cm^{-1} and the gypsum line at 1085 cm^{-1} while aiming at chemically modified statues/buildings. The upper part of Fig. 4.10 shows that the wavelength shift using 355 nm laser radiation results in a Raman peak separation of 1 nm in comparison to a separation of around 5 nm when using 800 nm laser radiation.

The lower part of Fig. 4.10 shows the wavelength distance of the above mentioned Raman peaks to the excitation wavelength. A longer excitation wavelength results in a larger separation between the closest Raman peak and the laser peak, which facilitates the choice of rejection filter.

The wavelength-shift between the two close-lying excitation wavelengths should be chosen to produce a large enough shift of the Raman peaks to give a strong signal after the subtraction. Also, if the wavelength-shifting is supposed to occur on a shot-to-shot basis, the shift must be within the limit for fast wavelength tuning (see Sect. 3.3.1). The optimum shift should induce a shift equal to the width of the investigated Raman peak, resulting in a derivative-like spectrum. The width of the Raman peaks depends strongly on the resolution of the detector and has to be investigated before the shift can be set.

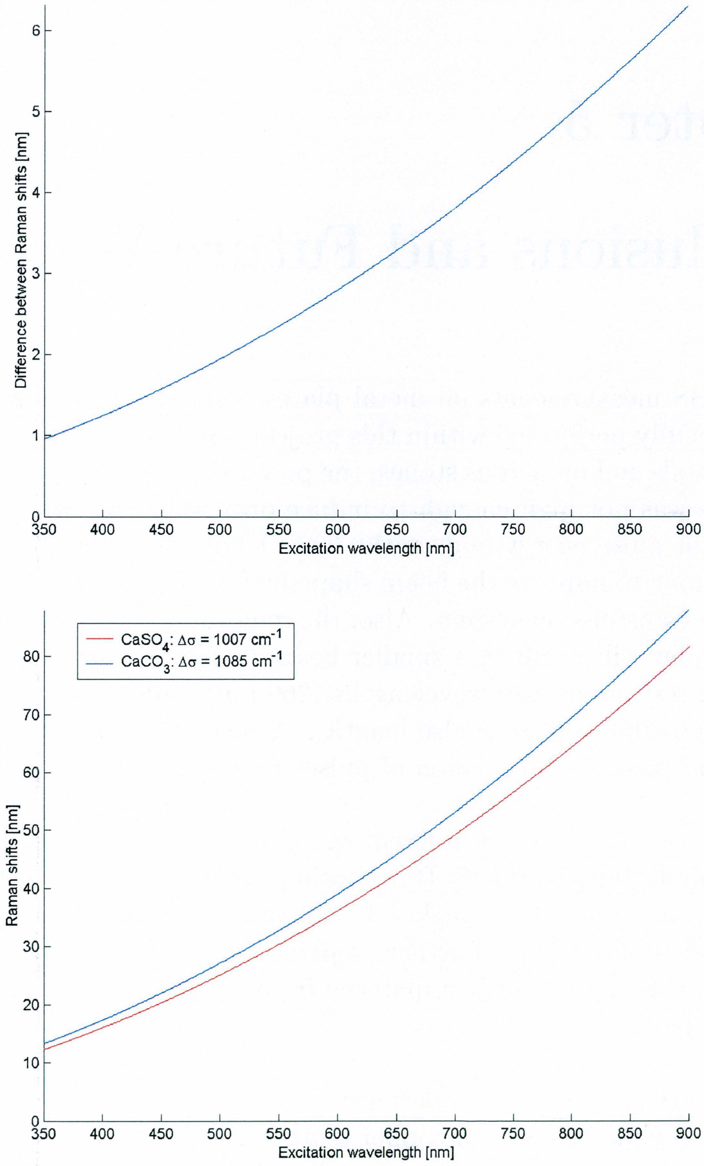

Figure 4.10: Wavelength difference between the Raman shifted peaks from $CaSO_4$ and $CaCO_3$ (top) and the distance from the excitation wavelength to both peaks (bottom).

Chapter 5

Conclusions and Future Work

Remote LIBS measurements on metal plates, stones, minerals and crystals were successfully performed within this project. However, in some cases such as SiO_2 crystals and numerous stones, the power density produced on the target surfaces was not high enough to induce optical breakdown. This is due to insufficient pulse energy and/or the large beam diameter. Optimizations need to be done to improve the beam shape by further alignment of the beam through the transmission system. Also, the removal of the astigmatism in the beam expander will result in a smaller beam diameter. Other natural steps would be to test other laser wavelengths (266 nm), different target distances and, when possible, shorter pulse lengths. A new and more durable folding mirror would permit transmission of pulses with higher energy.

False-colour coded images of different metal plates were obtained after performing Remote Imaging LIBS. By choosing smaller intervals, which exactly cover the strong fluorescence peaks, the discrimination between different materials would be improved. Further, sophisticated software could be developed to automatically identify a material from a database and then correctly colour the pixels.

Remote Ablative Cleaning was performed on an Italian statue replica and a statue head. Oxide layers on a copper plate and other crusts/layers on mortar and alabaster could also be removed with both spectroscopic guidance and self-terminating procedures. Finally, a discussion on how future Remote Raman measurements can be performed was included and directions given on what should be considered when choosing excitation wavelength, rejection filters and wavelength shift. Successful measurements could pave the way for a very exciting technique – Remote Imaging Raman Spectroscopy.

Chapter 6

Acknowledgements

This project could not have been done without the help of my first supervisor Rasmus Grönlund. Thank you for all the wonderful times in the LIDAR truck and for all the good advice given while I was writing the thesis. I hope I did a good job being your assistant during the measurements. Good luck with the future measurements!

I would like to thank my second supervisor Professor Sune Svanberg for giving me the opportunity to write this thesis at the Atomic Physics Division and for his inspiration through the years. Your guidance and encouragement has been highly appreciated while planning and performing the measurements.

A big thank you to the rest of the Molecular Spectroscopy Group – Magnus Bengtsson, Linda Persson, Mikael Sjöholm, Mats Andersson, Tomas Svensson and Gabriel Somesfalean for taking good care of me and for the nice Friday meetings. Also, I will never forget the great times with the African guest researchers - Benjamin Anderson (Ghana) and Gathoni Robinson (Kenya).

I would like to thank my good friends in Gröstorp (Daniel, Maria, Julia and Linus) for helping me collect minerals and crystals at the old silver mine and for all the cosy and entertaining weekends we have spent together.

I would also like to thank Professor Per-Gunnar Andréasson at the GeoBiosphere Science Centre, Lund University, for identifying the minerals and crystals.

Last but not least, I would like to thank Åke Bergquist for helping me out in the truck and Bertil Hermansson for the computer assistance.

Chapter 7

List of Acronyms

BBO	β-Barium Borate
CCD	Charged Coupled Device
DIAL	DIfferential Absorption LIDAR
HeNe	Helium-Neon
IR	InfraRed
LASER	Light Amplification by Stimulated Emission of Radiation
LIBS	Laser Induced Breakdown Spectroscopy
LIDAR	LIght Detection And Ranging
LIF	Laser Induced Fluorescence
LIPS	Laser Induced Plasma Spectrometry
MIDP	Mars Instrument Development Program
Nd	Neodymium
OMA	Optical Multi-channel Analyser
OPO	Optical Parametric Oscillator
R-LIBS	Remote Laser Induced Breakdown Spectroscopy
UV	UltraViolet
XRF	X-Ray Fluorescence
YAG	Yttrium Aluminium Garnet

Bibliography

[1] P. Weibring. *Environmental Monitoring by Multi-Spectral Lidar Techniques.* PhD Thesis, Lund Reports on Atomic Physics, LRAP-284, 2002.

[2] S. Svanberg. *Atomic and Molecular Spectroscopy - Basic Aspects and Practical Applications.* Springer-Verlag, 3rd Ed., 2001.

[3] L.J. Radziemski. From LASER to LIBS, the path of technology development. *Spectrochim. Acta Part B* ***57***, pages 1109–1113, 2002.

[4] O. Svelto. *Principles of Lasers.* Kluwer Academic/Plenum Press, 4th Ed., 1998.

[5] F.L. Pedrotti, S.J. and L.S. Pedrotti. *Introduction to Optics.* Prentice Hall International, 2nd Ed., 1996.

[6] Applied Photonics Limited. An Introduction to Laser-Induced Breakdown Spectroscopy. *http://www.appliedphotonics.force9.co.uk/About_LIBS/about_libs.html.*

[7] International School of Photonics. Laser Induced Plasma Spectroscopy. *http://www.photonics.cusat.edu/Research_Laser%20Induced%20Plasma.html.*

[8] D.A. Rusak, B.C. Castle, B.W. Smith, and J.D. Winefordner. Recent trends and the future of laser-induced plasma spectroscopy. *Trends in Anal. Chem.* ***17***, pages 453–461, 1998.

[9] S. Palanco and J. Laserna. Remote sensing instrument for solid samples based on open-path atomic emission spectrometry. *Rev. Sci. Instr.* ***75***, pages 2068–2073, 2004.

[10] R.C. Wiens, D.A. Cremers, M. Ferris, J.E. Nordholt, J.D. Blacic, P. Lucey, and S.K. Sharma. Development of a Prototype Laser-Induced Breakdown Spectroscopy (LIBS) Instrument with Stand-Off Raman Capabilities as Part of the Mars Instrument Development Program. *Lunar and Planetary Science XXXI* ***1468***, 2000.

[11] S.M. Angel, D.N. Stratis, K.L. Eland, T. Lai, M.A. Berg, and D.M. Gold. LIBS using Dual- and Ultra-Short Laser Pulses. *Anal. Chem.* ***369***, pages 320–327, 2001.

[12] K.L. Eland, D.N. Stratis, D.M. Gold, S.R. Goode, and S.M. Angel. Energy Dependence of Emission Intensity and Temperature in a LIBS Plasma Using Femtosecond Excitation. *Appl. Spectrosc.* ***55***, pages 286–291, 2001.

[13] Ph. Rohwetter, J. Yu, G. Méjean, K. Stelmaszczyk, E. Salmon, J. Kasparian, J.-P. Wolf, and L. Wöste. Remote LIBS with ultrashort pulses: Characteristics in picosecond and femtosecond regimes. *J. Anal. At. Spectrom.* ***19***, pages 437–444, 2004.

[14] C.M. Davies, H.H. Telle, D.J. Montgomery, and R.E. Corbett. Quantitative analysis using remote laser-induced breakdown spectroscopy (LIBS). *Spectrochim. Acta Part B* ***50***, pages 1059–1075, 1995.

[15] Office of Industrial Technologies Energy Efficiency and Renewable Energy U.S. Department of Energy. Mine compatible laser analysis instrument for ore grading. *http://www.oit.doe.gov/mining*, 2001.

[16] J.L. May, J. Alexander Idaho National Engineering, and Environmental Laboratory (operated by U.S. Department of Energy). Development of a Mine Compatible LIBS for Ore Grading. *http://energy.inel.gov/mining/documents/ore-grading.pdf*.

[17] P. V. Maravelaki, V. Zafiropulos, V. Kilikoglou, M. Kalaitzaki, and C. Fotakis. Laser-induced breakdown spectroscopy as a diagnostic technique for the laser cleaning of marble. *Spectrochim. Acta Part B* ***52***, pages 41–53, 1997.

[18] W.-B. Lee, J. Wu, Y.-I. Lee, and J. Sneddon. Recent Applications of Laser-Induced Breakdown Spectrometry: A Review of Material Approaches. *Appl. Spectrosc. Rev.* ***39***, pages 27–97, 2004.

[19] A.K. Knight, N.L. Scherbarth, D.A. Cremers, and M.J. Ferris. Characterization of Laser-Induced Breakdown Spectroscopy (LIBS) for Application to Space Exploration. *Appl. Spectrosc.* ***54***, pages 331–340, 2000.

[20] Jet Propulsion Laboratory. NASA Mars Exploration Program. *http://marsprogram.jpl.nasa.gov/missions/future/msl.html*.

[21] A.I. Whitehouse, I.M. Botheroyd J.Young, S. Lawson, C.P. Evans, and J. Wright. Remote material analysis of nuclear power station steam generator tubes by laser-induced breakdown spectroscopy. *Spectrochim. Acta Part B* ***56***, pages 821–830, 2001.

[22] R.S. Harmon, F.C. De Lucia, A.W. Miziolek, A. LaPointe, R.J. Winkel, Jr, and R.A. Walters. The use of laser-induced breakdown spectroscopy to discriminate between landmines and other objects. *24th Army Science Conference Proceedings, Orlando, Florida*, 2004.

[23] S.B. Mirov, R.E. Pitt, A. Dergachev, W. Lee, D.V. Martyshkin, O.D. Mirov, J.J. Randolph, L.J. DeLucas, C.G. Brouillette, T.T. Basiev, Y.V. Orlovskii, and O.K. Alimov. A novel laser breakdown spectrometer for environmental monitoring. *Air Monitoring and Detection of Chemical and Biological Agents (edited by J. Leonelli and M.L. Althouse). SPIE* ***3855***, pages 34–41, 1999.

[24] P.L. García, J.M. Vadillo, and J.J. Laserna. Real-Time Monitoring of High-Temperature Corrosion in Stainless Steels by Open-Path Laser-Induced Plasma Spectrometry. *Appl. Spectrosc.* ***58***, pages 1347–1352, 2004.

[25] C.M. Stellman and F. Bucholtz. Suppression of Fluorescence Interference via Wavelength Shift-Keyed Raman Spectroscopy using an Argon Ion Laser and Acousto-Optic Tunable Filter. *Spectrochim. Acta Part A* ***54***, pages 1041–1047, 1998.

[26] P. Mazzinghi and F. Margheri. A short pulse, free running, Nd:YAG laser for the cleaning of stone cultural heritage. *Opt. Lasers Eng.* ***39***, pages 191–202, 2003.

[27] H.W. Hubble, M. Ghosh, S.K. Sharma, K.A. Horton, P.G. Lucey, S.M. Angel, and R.C. Wiens. A combined remote LIBS and Raman spectroscopic study of minerals. *Lunar and Planetary Science XXXIII* ***1935***, 2002.

[28] N. Gupta and R. Dahmani. AOTF Raman Spectrometer for Remote Detection of Explosives. *Spectrochim. Acta Part A* ***56***, pages 1453–1456, 2000.

[29] P. Weibring, H. Edner, and S. Svanberg. Versatile mobile lidar system for environmental monitoring. *Appl. Opt.* ***42***, pages 3583–3594, 2003.

[30] R. Grönlund. Technology Adaptations for Improved Multi-Spectral LIDAR Measurements. Master's thesis, Lund Reports on Atomic Physics, LRAP-296, February 2003.

[31] P. van Walree. Vignetting. *http://www.vanwalree.com/optics/vignetting.html*.

[32] C. af Klinteberg, M. Andreasson, O. Sandström, S. Andersson-Engels, and S. Svanberg. Compact medical fluorosensor for minimally invasive tissue characterization. *Rev. Sci. Instr.* ***76***, *034303*, pages 1–6, 2005.

[33] D.R. Lide. *CRC Handbook of Chemistry and Physics*. CRC Press, Boca Raton, Florida, 74th Ed., 1993.

[34] R. Grönlund, M. Bengtsson, J. Hällström, M. Sjöholm, G. Somesfalean, T. Johansson, P. Weibring, H. Edner, K. Barup, and S. Svanberg. Lidar remote-sensing assessment of the cultural heritage using laser-induced fluorescence and laser-induced break-down spectroscopy. *Air Pollution and Cultural Heritage, C. Saiz-Jimenez (ed.), A.A. Balkema, Netherlands*, pages 167–170, 2004.

[35] J. Ralph. Mineralogy Database. *http://www.mindat.org/*.

A. Appendix A

Remote imaging laser-induced break-down spectroscopy and remote cultural heritage ablative cleaning

Rasmus Grönlund, Mats Lundqvist and Sune Svanberg
Atomic Physics Division, Lund Institute of Technology
P.O. Box 118, S-221 00 Lund, Sweden

Abstract: We report, what we believe to be for the first time, on remote imaging laser-induced breakdown spectroscopy (LIBS). Measurements have been performed using a tripled Nd:YAG laser working at 355 nm with 170 mJ pulse energy that is expanded and focused onto a target at 60 m distance. The LIBS signal is detected using an on-axis Newtonian telescope and an optical multichannel analyzer. The imaging is performed by scanning the laser beam on the target. The same set-up could readily be used for remote laser ablation for cleaning of contaminated objects with application towards the cultural heritage.

Laser-induced breakdown spectroscopy (LIBS) is a powerful method for material elemental analysis based on emission spectroscopy[1,2]. It has been widely applied in analytical chemistry[3]. LIBS can be applied remotely as demonstrated in early Russian work and more recently by Palanco *et al.*[4], Rohwetter *et al.*[5] and ourselves[6]. Lidar (light detection and ranging) techniques were employed using CO_2, Nd:YAG and short-pulse femtosecond laser systems. The remote detection from selected spots was demonstrated. In a parallel development, remote LIBS is now being developed for deployment on remotely operated Mars landing vehicles[7].

Laser ablation, where laser pulses are employed for explosive evaporation of small amounts of surface materials, is a widely used technique for micro-machining and thin-film fabrication. It is also used for surface cleaning in the field of cultural heritage management, e.g. of paintings or statues[8].

Laser-induced fluorescence (LIF) is a widely used technique for environmental monitoring and tissue diagnostics in medicine (see e.g. Ref. 9). Recently, remote LIF of monument facades has been demonstrated with fluorescence lidar systems[10,11] and imaging in combination with multi-variate analysis provides new possibilities for the characterization of stone surfaces[11,12]. Objects studied include the Lund Cathedral, the Parma Cathedral and Baptistery, and the Coliseo and Lateran Baptistry in Rome.

Remote imaging LIBS and remote ablative cleaning of stone surfaces are described in the present Letter, as we believe, for the first time. The Lund mobile lidar system, which was recently thoroughly up-graded[13], was used in the present work. The experiments were performed with a system-target distance of 60 m. The important aspects of the lidar system regarding the present work on LIBS and remote ablation are presented in Fig. 1. We use frequency-tripled radiation (355 nm) from a 20 Hz pulsed Nd:YAG laser, and the radiation is transmitted towards the target via a 10 cm diameter specially designed refractive transmission telescope placed coaxially with the receiving 40 cm diameter reflective Newtonian telescope. The transmission and receiving beam paths are folded via a roof-top 40x80 cm first surface aluminized mirror, which is controlled by stepper motors for precision scanning of the target.

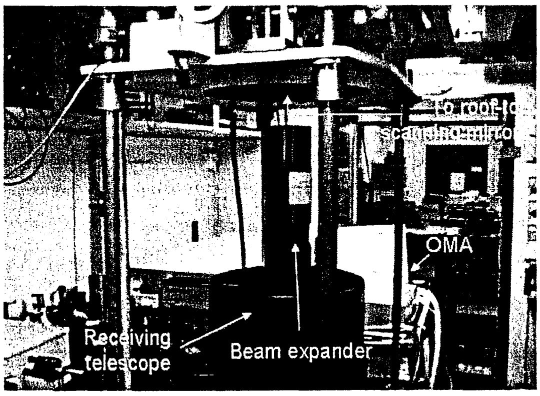

Fig. 1. The measurement set-up with the important parts of the interior of the lidar system.

A key aspect in remote LIBS and remote surface ablation is to ensure that sufficiently high optical field strength can be achieved in the remote focus to induce a plasma break down at the solid target surface. Clearly, due to diffraction, the laser beam must first be expanded and transmitted through a low-aberration telescope which we designed with the aid of a ray-tracing program (Linos Photonics, WinLens 4.3). Basically, one planoconcave and two planoconvex lenses with focal lengths of, -25, 500 and 1000 mm and spaced by ~20 and ~25 cm were employed. The beam diameter and the laser pulse energy chosen must be matched in such a way, that a laser spark is induced at the target without causing optical damage, especially to the aluminized folding mirror. We normally employed 170 mJ, 4-5 ns long pulses at 355 nm, generated by a Spectra-Physics Model GCR-290 Nd:YAG laser. While a focal-spot diameter of about 0.7 mm at a 60 m distant target is calculated, we in practice noted burn-marks with a diameter of about 5 mm. The selection of tripled Nd:YAG radiation instead of doubled (532 nm) or fundamental (1064 nm) radiation is governed by improved break-down characteristics for short-wavelength radiation and eye-safety considerations (outside the focus the UV beam comparatively fast reaches eye-safe intensity levels). Further, the use of UV radiation allows plasma light to be detected throughout the visible region and fluorescence can also be efficiently induced. As a comparison 25 mJ 355 nm pulses transmitted by a 5 cm telescope are normally used in lidar fluorescence imaging[11,12].

The plasma light, collected by the lidar receiving telescope is focused into a 600 μm diameter optical fiber which is connected to the entrance slit of an Oriel Corporation MS125 400 lines mm^{-1} grating spectrometer equipped with an Andor DH50125U-01 gated and intensified ccd detector. The spectral region 360-800 nm is detected with a spectral resolution of 2.2 nm. The intensifier is activated with a temporal window of typically 150 ns which can be temporally located to match the arrival of the prompt target emission or be delayed to observe the plasma afterglow.

The present measurements were performed in Lund with the lidar system parked at the Physics Department, with the target area located on an easily accessible roof and with a brick wall terminating any stray laser pulses. Laser pulses are transmitted from the lidar roof-top mirror 4 m above the ground level in a completely safe manner. The lidar system is equipped with two TV cameras surveying the target area through the roof-top transmission dome with clear marking of the exact target spot. As targets, arrangements of metal plates made of different elements were used. In addition, stone samples and even statues were utilized.

As a first example of remote LIBS spectra we show in Fig. 2 emission lines from copper and aluminum targets, recorded 300 ns after ablation with a 150 ns gate. The vertical lines correspond to tabular values of prominent emission lines of different elements[14]. Note that magnesium and sodium contamination can be seen in the aluminum case.

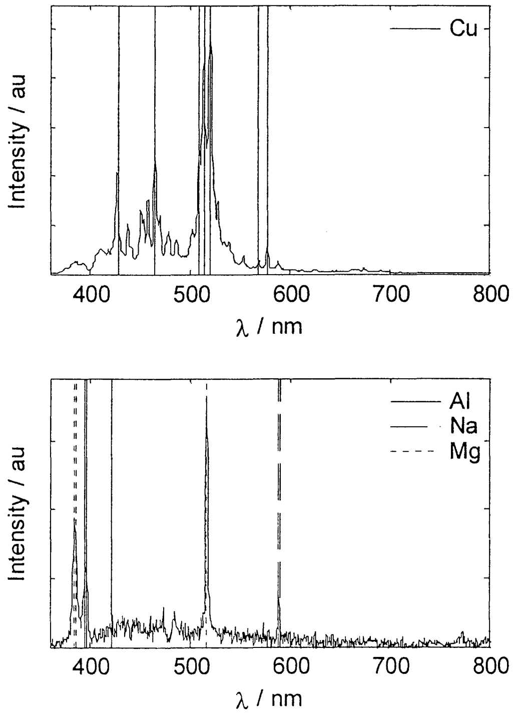

Fig. 2. Remote LIBS spectra from metal plates of copper and aluminum. The vertical lines correspond to tabular values of prominent emission peaks14. Note that magnesium and sodium contamination can be clearly seen in the aluminum case.

By scanning the laser beam under computer control it was possible to generate LIBS images such as shown in Fig. 3. A photograph of the target is included. By image processing looking at the characteristic lines of different elements it was possible to identify the target materials as shown in the figure.

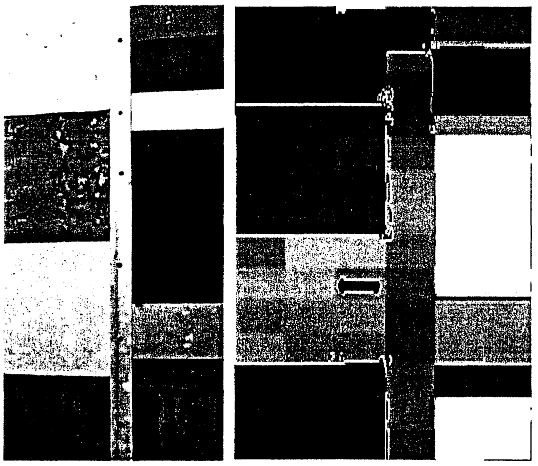

Fig.3. LIBS imaging of metal plates, the target on the left and a false-color coded identification image on the right with copper (red), aluminum (green) and iron (blue). The classification has good correspondence to the spots where the laser has hit the target. The big plates on the left are (downwards): stainless steel, brass, aluminum and iron. The stainless steel is classified as iron and the brass as copper as they contain large amounts of these substances. The vertical profiles holding the plates are made of aluminum and classified accordingly. Note that the pixels are much larger than the spot size and that the scanning resolution is quite low. The beam scanning has been slightly tilted, and the middle spot in the top row does not hit the aluminum profile but the stainless steel plate. White parts correspond to non-metallic surfaces.

The energy deposited in the plasma is sufficient to perform ablation and surface layer removal. On metal targets clear ablation marks could be seen. Oxide layers could be removed, even green copper hydroxide typical of copper roofs at coast-line locations could be ablated. Surface layer removal from stone surfaces has considerable interest in terms of cultural heritage management. Thus, biodeteriogen layers on weathered mortar surfaces could be removed as well as corresponding coatings on granite rock (Fig. 4a). Pencil and marker-pen blackened areas on white alabaster slabs (Volterra, Italy) could be readily removed (Fig. 4b) at a working speed of about 10 cm^2 min^{-1}. The ablation process is basically self-terminating when the white substrate is reached. Here the samples were manually moved in a fixed beam. In order to perform a realistic remote cleaning of a statue, a 1 m tall white Italian garden replica statue partially covered by dirt and algal growth after 10 years of weather exposure was used as a target. The remote cleaning of the statue with computerized beam scanning is illustrated in Fig. 4c. Finally, an Italian replica statue head, made of white Carrara marble was exposed and an area heavily blackened by a soft pencil was cleaned (Fig. 4d). No detectable surface damage could be observed to the naked eye.

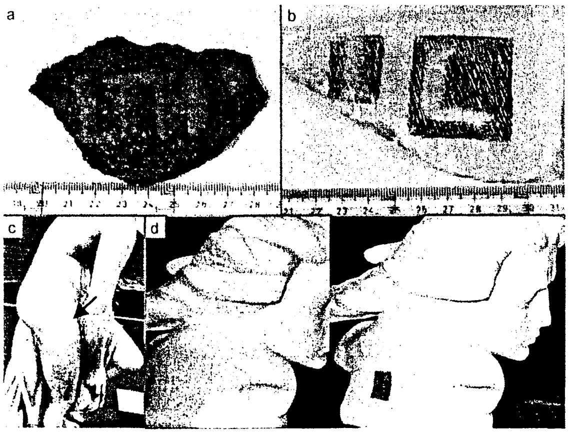

Fig. 4. Remote laser ablative cleaning of mortar (a), alabaster (b), a replica of an Italian statue with the arrow indicating the 100 cm2 cleaned area (c) and a statue made of Carrara marble after and before cleaning (d).

Fluorescence and line emission spectra could be expected to change as the ablation of the surface layer proceeds and the substrate is reached. Thus the spectroscopic signals might be used to control the ablation in a similar way as coronary artery ablation can be supervised by a spectroscopic signal recorded through the fiber used (see e.g. Ref. 15).

It should be noted, that the experiment described could, like in earlier LIF-lidar campaigns[11,12], have been performed at any historical monument, since the mobile lidar system is fully self-contained and is equipped with a 40 kVA motor generator towed by the lidar truck. The present work shows, that remote imaging LIBS can be used for surface assessment at considerable stand-off distance and thus constitutes a complement to remote fluorescence imaging, e.g. in the assessment of historical monuments. Further, remote laser ablation with spectroscopic guidance, seems to be a realistic possibility, which could reduce the cost of very expensive scaffolding in restoration work. Clearly, only areas directly seen from the ablation lidar system can be cleaned; however, these are on the other hand the only ones which are visible to the spectator.

This work was supported by the Swedish Research Council for Environment, Agricultural Sciences and Spatial Planning (FORMAS), and the Knut and Alice Wallenberg Foundation. Valuable assistance from Gabriel Somesfalean, Magnus Bengtsson and Hans Edner in the early stage of the experiment is gratefully acknowledged.

References

1. L.J. Radziemski, T.R. Loree, D.A. Cremers, and N.M. Hoffman, Anal. Chem. **55**, 1246 (1983).
2. D.A. Cremers and L.J. Radziemski, in *Laser Spectroscopy and its Applications*, L.J. Radziemski, R.W. Solarz, and J.A. Paisner (eds.) (Dekker, New York, 1989)
3. Special issue on LIBS: Spectrochim. Acta B **56**, 565 (2002)

4. S. Palanco, J.M. Baena, and J.J. Laserna, Spectrochim. Acta B **57**, 591 (2002)
5. Ph. Rohwetter, J. Yu, G. Méjean, K. Stelmaszczyk, E. Salmon, J. Kasparian, J.P. Wolf and L. Wöste, J. Anal. At. Spectrom. **19**, 437 (2004)
6. R. Grönlund, M. Bengtsson, M. Sjöholm, G. Somesfalean, T. Johansson, P. Weibring, H. Edner, S. Svanberg, J. Hällström, K. Barup, in C. Saiz-Jimenez (ed.), *Air Pollution and Cultural Heritage* (A.A. Balkema, Netherlands, 2004)
7. R.C. Wiens, S. Maurice, D.A. Cremers, and S. Chevrel, Lunar and Planetary Science XXXIV, 1646 (2003)
8. C. Fotakis, S. Georgiou, V. Zafiropulos and V. Tornari, SPIE **4402**, 8 (2001)
9. S. Svanberg, *Atomic and Molecular Spectroscopy – Basic Aspects and Practical Applications*, 4th Edition (Springer, Heidelberg, Berlin, New York, 2004).
10. V. Raimondi, G. Cecchi, L. Pantani, and R. Chiari, Appl. Opt. **37**, 1089 (1998).
11. P. Weibring, Th. Johansson, H. Edner, and S. Svanberg, B. Sundnér, V. Raimondi, G. Cecchi, and L. Pantani, Applied Optics **40**, 6111 (2001).
12. D. Lognoli, G. Cecchi, I. Mochi, L. Pantani, V. Raimondi, R. Chiari, Th. Johansson, P. Weibring, H. Edner and S. Svanberg, Appl. Physics B **76**, 457 (2003).
13. P. Weibring, H. Edner and S. Svanberg, Applied Optics **42**, 3583 (2003).
14. D.R. Lide (ed.), *CRC Handbook of Chemistry and Physics* (CRC Press, Boca Raton, Florida, 74th edition 1993).
15. S. Svanberg, Phys. Scr. **T72**, 69 (1997)

B. Appendix B

Remote LIBS and Raman Imaging for Assessment of Cultural Heritage

Rasmus Grönlund, Magnus Bengtsson, Mats Lundqvist, Gabriel Somesfalean and Sune Svanberg
Atomic Physics Division, Lund Institute of Technology, P.O. Box 118, 221 00 Lund, Sweden
http://www-atom.fysik.lth.se

LIBS is an abbreviation for Laser-Induced Breakdown Spectroscopy and is widely used in laboratory environments for analysis of the chemical contents of a material. Raman radiation is received when atoms or molecules are excited from a low-lying level to a virtual level and quickly relaxes back to a close-lying, but not the same, lower state. The re-emitted light is then changed in wavelength, either upwards (Stokes) or downwards (Anti-Stokes). We propose to perform remote LIBS and Raman imaging of historical monuments to assess the state of a building.

The truck-borne lidar system of the Lund Institute of Technology [1] is primarily developed for monitoring of atmospheric pollutants, but is also well suited for these kinds of measurements. The system is equipped with a Nd:YAG-pumped optical parametrical oscillator (OPO) system, allowing laser radiation in the wavelength range 220 nm-4 µm to be created. The laser radiation can be sent through a roof-top dome which can steer the radiation onto the point of interest. In this way imaging in both LIBS and Raman mode can be performed.

LIBS is performed using tripled Nd:YAG laser radiation at 355 nm. The beam is expanded to ~10 cm diameter in a beam expander system where the lenses can be moved relative to each other, allowing focusing at the desired distance (~50-100 m). The challenge is achieving sufficiently high energy density at the target to induce breakdown. The LIBS signal is detected using a 40-cm-diameter Newtonian telescope and focused onto an optical fibre end and transmitted into an optical multichannel analyzer system. The CCD is gated to select emission of a chosen time delay and also to suppress background radiation. We have already performed "quasi-remote" LIBS by using a focusing lens close to the studied material, giving interesting signals as seen in Fig. 1 and comparison with [2] gives confidence that our setup should work.

The Raman signal is often drenched in the much stronger fluorescence signal, and fluorescence modeling is often used to retrieve the desired signal. However, using the OPO system the wavelength can be changed by a small amount (~3 nm) which will leave the fluorescence unchanged whereas the Raman signal will move accordingly. The ratio between the two curves can then be formed, creating a derivative-kind function of the Raman signal and removing the fluorescence. The Raman signal is very weak and thus averaging over many shots is required to enhance the signal-to-noise ratio.

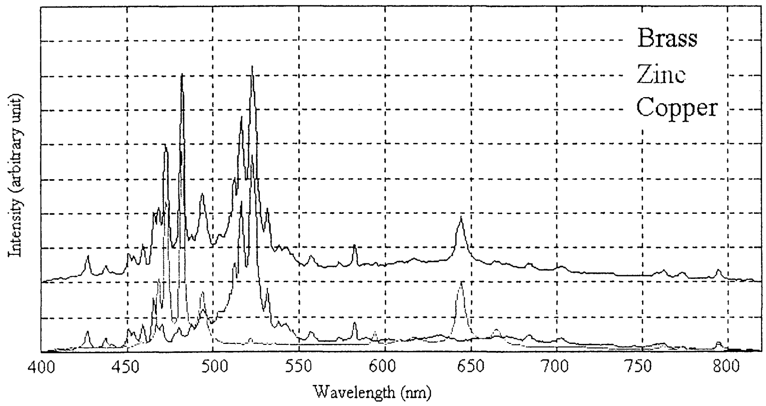

Figure 1. LIBS spectra from brass, Zn and Cu. The brass (alloy of Zn and Cu) curve is lifted for clarity.

[1] P. Weibring, H. Edner and S. Svanberg, *Versatile mobile lidar system for environmental monitoring*, Applied Optics **42** (2003) 3583

[2] S. Palanco, J.M. Baena, J.J. Laserna, *Open-path laser-induced plasma spectrometry for remote analytical measurements on solid surfaces*, Spectrochimica Acta Part B **57** (2002) 591